Journal of

Computation and Artificial Intelligence in Mechanics and Biomechanics

Editor in Chief:
Jorge Belinha

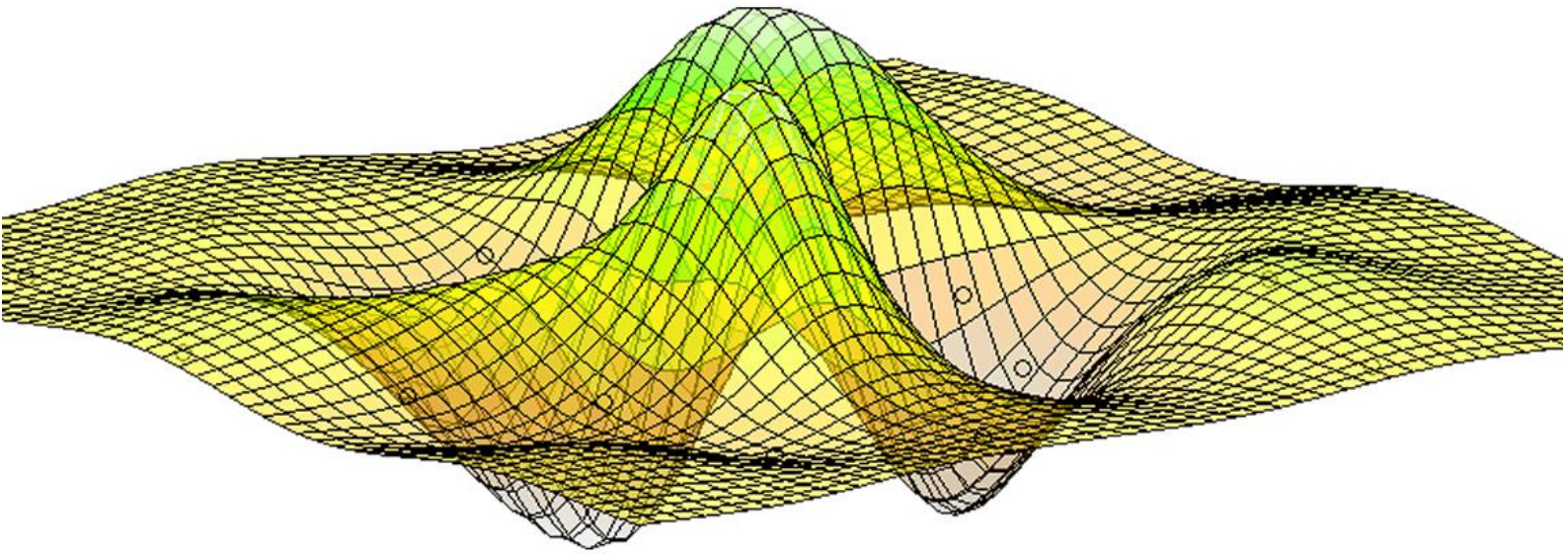

ISSN 2184-8971
Volume 1, Issue 2

PUBLICAÇÕES ISEP
European Commission | Horizon 2020 European Union funding for Research & Innovation
OpenAIRE
zenodo

Journal of Computation and Artificial Intelligence in Mechanics and Biomechanics

Editorial overview by
Editor in chief: Jorge Belinha [1]

[1]*School of Engineering, Polytechnic of Porto (ISEP), Department of Mechanical Engineering, Portugal, job@isep.ipp.pt*

Journal of Computation and Artificial Intelligence in Mechanics and Biomechanics (JCAIMB) is a scholarly online peer review free open access journal fully sponsored by "Publicações ISEP". All manuscripts are available in the ZENODO repository database, from OpenAIRE project, allowing an automatically abstracting and indexation and free open access.

Thus, JCAIMB is committed to ensure free Open Science to both authors and readers and to publish only quality works, which are reviewed by experts in related field. Thus, JCAIMB aims to publish quality original research works, following the scientific method of scholarly value in computational mechanics and biomechanics combined with several degrees of artificial intelligence, whose formulations and applications are properly demonstrated and validated. Nevertheless, innovative applications using commercial software packages are encouraged, as well as original and up-to-date revision manuscripts. In this issue, four manuscripts are published in JCAIMB:

- Stress analysis of skin wounds using advanced discretization techniques, by Ana Guerra, Jorge Belinha and Renato Natal Jorge;
- Estimating active forearm pronation-supination motion by means of FE modelling, by I.J. Sánchez-Arce;
- Influence of middle ear tumours on the biomechanical behaviour of the chorda tympani, by Leonor Mendonça, Carla F. Santos, Fernanda Gentil, Marco Parente, Bruno Areias and Renato Natal Jorge;
- Biomechanical study of the shoulder joint complex and associated injuries, by Catarina Silva, João Ferreira and Marco Parente.

Enjoy.

The editorial team.

Technical information:

Publisher:	Publicações ISEP - https://publicacoes.isep.ipp.pt/
Repository:	ZENODO repository database - https://zenodo.org/
Licence:	under the terms of the Creative Commons Attribution 4.0 International (CC BY 4.0) license.
Director:	Jorge Belinha
Email:	job@isep.ipp.pt
Format:	Online: https://publicacoes.isep.ipp.pt/jcaimb
Periodicity:	Semestrial

Journal of Computation and Artificial Intelligence in Mechanics and Biomechanics ISSN 2184-8971
Volume 1, Issue 2, Page 29-35, 2021

Stress analysis of skin wounds using advanced discretization techniques

Ana Guerra [1], Jorge Belinha [2], Renato Natal Jorge [3]

[1] *aguerra@inegi.up.pt; INEGI, Rua Dr. Roberto Frias, 400, 4200-465; Porto; Portugal*
[2] *job@isep.ipp.pt; ISEP, Rua Dr. António Bernardino de Almeida, 431, 4249-015; Porto; Portugal*
[3] *rnatal@fe.up.pt; FEUP, Rua Dr. Roberto Frias, 4200-465 Porto, Portugal*

Abstract

Human skin is the largest human organ and it is an important physical barrier that allows body homeostasis. During wound healing, this mechanically flexible organ is capable to repair itself. Nevertheless, the wound represents an abrupt change in the skin continuum, leading to stress concentrations in the surrounding wound area. Advanced discretization techniques, namely finite element method (FEM) and radial point interpolation method (RPIM), are suitable computational tools to simulate biomechanical problems allowing to analyse the displacement field and the corresponding stress and strain fields. This study aimed to construct a 2D model of skin wounds with different depths and to analyse the stress and strain fields obtained, using FEM and RPIM analysis. The simulations results demonstrated that the highest levels of stress were observed in the end of the wound, in both techniques used. Regarding the strain fields, hypodermis presented the highest values. Although this is a preliminary study to assess the performance of these numerical methods in the analysis of stress profile distribution in the human skin, it was possible to conclude that both finite element method and radial point interpolation method are valid numerical tools. Moreover, the materials used in the simulations were well characterized in terms of elasticity. In future work, it is intended to refine the model parameters and to include the hyperelastic and the anisotropic behaviour of the human skin.

***DOI**: 10.5281/zenodo.4837321*

Article Info

Keywords
Finite element method
Radial Point Interpolation Method
Human skin
Stress and strain fields

Article History
Received: 02/11/2020
Revised: 30/01/2021
Accepted: 25/03/2021

1 Introduction

Skin wounds can be the consequence of damage in traumatic accidents, the result of surgical incisions or of long periods of immobility or they can be associated with other pathologies, such as obesity and diabetes. Given its high frequency during human life, the treatment of skin wounds presents high economic and social costs in our society [1, 2].

Human skin is an important physical barrier between the body and the external environment. This tissue is composed by two layers: epidermis and dermis. The epidermis, the upper layer, is very thin being minimal its contribution to the mechanical behaviour of the skin. The dermis, the layer below the epidermis, has approximately 2 mm of thickness and provides the structural and the nutritional support for the skin. The dense collagen and elastin network in the dermis is responsible for the skin's mechanical properties [3]. Although not consensual, a third layer can be considered, the hypodermis, mainly composed by fat connective tissue that connects the dermis with the skeletal components. Each skin layer presents its own composition well defined and its specific mechanical properties.

When the skin is damaged wound healing takes place in order to restore the tissue homeostasis. Wound healing is usually divided in four phases: haemostasis, inflammation, proliferation and tissue remodelling [4]. For the correct skin wound healing this orderly sequence of events have to occur. Otherwise, if any step of the healing process is changed, pathogenic responses may take place leading to fibrosis or chronic wounds. In fact, injuries in the skin normally results in changes in the skin composition and in the scar formation. Scars present different mechanical response comparatively to healthy tissue. Therefore, skin wounds represent an abrupt change in the skin continuum, leading to stress concentrations in the surrounding of the wound area.

Skin computational modelling received more attention in the last few years. Indeed, computational modelling is a useful tool in surgery planning and treatment optimization [5, 6]. Some authors used advanced discretization techniques, namely finite element method (FEM) and meshless methods to predict the geometry of surgical incisions [7] and to analyse stress distribution in the skin [8] in order to reduce scar formation. In the future, it is intended that advanced discretization techniques could assist surgeons in the decision-making process when planning individual surgeries,

Corresponding Author:
Ana Guerra
aguerra@inegi.up.pt

allowing to establish the regions with stress and strain concentration in order to improve the skin wound healing and the scar formation.

As already mentioned, stress is one of the many biological factors that plays an important role in wound healing and in scar formation. Accordingly, analyse stress theoretically is demanded, since no invasive or non-invasive technique to measure stress directly is available. It has already been shown that minimum stress is useful for producing a better scar. However, maximum stress has adverse effects in wound healing and compressive stress should be avoided since skin cannot support negative stress. Moreover, excessive tissue tension can compromise blood supply and consequently promote tissue necrosis [9]. Therefore, analysing the stress profile distribution in the skin after wounds occurrence is very important in order to address new and more effective therapies. However, as already discussed, there are no invasive or non-invasive methodologies to measure stress *in vivo* [10]. Thus, advanced discretization techniques provide an excellent alternative to predict tissue stress.

In this work, we constructed 2D models of skin wounds with different depths and we performed a linear elasto-static analysis of the stress and strain fields obtaining in each model, using both FEM and Radial Point Interpolation Method (RPIM). Moreover, the efficiency of both numerical methods used will be addressed.

2. Numerical analysis

FEM and RPIM methods are very well implemented due to their application in several areas and their possibility to deal with complicated geometries, loads and different material properties.

In FEM the domain is discretized with a finite number of interconnected elements. FEM is a mesh-dependent method, in which every element is connected, directly or indirectly, to every other elements constructing a mesh. In the generic procedure, first it is necessary to obtain the discretized mesh and then the interpolation function should be achieved. The polynomials functions are used to interpolate the field variables over the element. Then, the Galerkin method is used to obtain the discrete equation system. To find the global equation system, the local element equations for all elements used for the discretization need to be combined. Before performed the solution, the boundary conditions should be imposed. Finally, it is possible to solve the global equation system [11].

In RPIM, the problem domain is discretized with a free nodal distribution and the field functions are approximated within an influence-domain rather than an element [12, 13]. Since there is no predefined nodal interdependency in RPIM, the nodal connectivity has to be enforced after the nodal discretization. Consequently, the 'influence-domain' of each node, obtained by searching enough nodes inside of a fixed area, is determined. In meshless methods, the nodal distribution does not form a mesh, since the only information previously required is the spatial location of each node that discretize the problem domain. A fine nodal distribution leads, generally, to accurate results. However, the increase in the total number of nodes also increase the computational cost. Once the nodal discretization is completed, the background integration mesh should be constructed. This is necessary to numerically integrate the weak form equations governing the physic phenomenon under study. Accordingly, the integration mesh, using the Gauss-Legendre quadrature scheme, is constructed. The following step consists in establish the discrete equation system, using the approximation or interpolations shape functions. In RPIM, the interpolation shape function combines a radial basis function with a polynomial basis function to obtain the approximation. The interpolation functions possess the Kronecker delta property, which means that the obtained function passes through all scattered points in the influence domain. Accordingly, this property simplify the imposition of the essential boundary conditions [12].

3. Solid mechanics

The solids and structures become stressed when they are subject to loads or forces. This stress results in strain, which can be interpreted as deformation or relative displacements [12]. The relationship between stress and strain and the relationship between strain and displacements are the focus of solid mechanics. In this work, only linear elastic materials are considered. It means that the relationship between stress and strain is assumed to be linear and the deformation in the solid caused by loading disappears fully with the unloading. Moreover, all the materials were considered to exhibit isotropic behaviour. For this reason, the materials can be completely defined by its Elastic Modulus (E) and Poisson's coefficient (ν). Furthermore, the relationship between the components of stress and strain can be given by the Hooke's Law.

The present work was developed in two-dimensions, considering the plane strain or the plane stress assumptions. In this work we aim to analyse the von Mises stress and the equivalent strain obtained in skin. Accordingly, the von Mises stress for each interest point, $\boldsymbol{x}_I$, can be calculated using Eq.(1) and the equivalent strain for each interest point, $\boldsymbol{x}_I$, can also be obtained using Eq.(2). The fully description of all the concepts and formulation in this area is presented in [12].

$$\bar{\sigma}(\boldsymbol{x}_I) = \sqrt{\frac{1}{2}[(\sigma(\boldsymbol{x}_I)_1 - \sigma(\boldsymbol{x}_I)_2)^2 + (\sigma(\boldsymbol{x}_I)_2 - \sigma(\boldsymbol{x}_I)_3)^2 + (\sigma(\boldsymbol{x}_I)_3 - \sigma(\boldsymbol{x}_I)_1)^2]} \quad (1)$$

$$\bar{\varepsilon}(\boldsymbol{x}_I) = \sqrt{\frac{2}{3}[(\varepsilon(\boldsymbol{x}_I)_1 - \varepsilon_m)^2 + (\varepsilon(\boldsymbol{x}_I)_2 - \varepsilon_m)^2 + (\varepsilon(\boldsymbol{x}_I)_3 - \varepsilon_m)^2]} \quad (2)$$

4. Numerical model

In this work, we developed 2D models to analyse the von Mises stress and the equivalent stain in wounds with different depths, using FEM and RPIM analysis. All the numerical simulations were performed using the software FEMAS. In Fig. 1 the geometry and boundary conditions used are presented. Concerning model A, the wound is located entirely in the dermis. In model B the wound is located in the transition from the dermis to the hypodermis. Finally, in model C the wound is located until the hypodermis. In all the three models the displacement (δ) was applied to all the elements localized in the boundary in the left side. It is equal to 10% of the wound depth in the top and zero in the bottom, and all the elements in the middle have the respective displacement value. In Table 1 the model dimensions and the material properties of each skin layer used to constructed the models are presented.

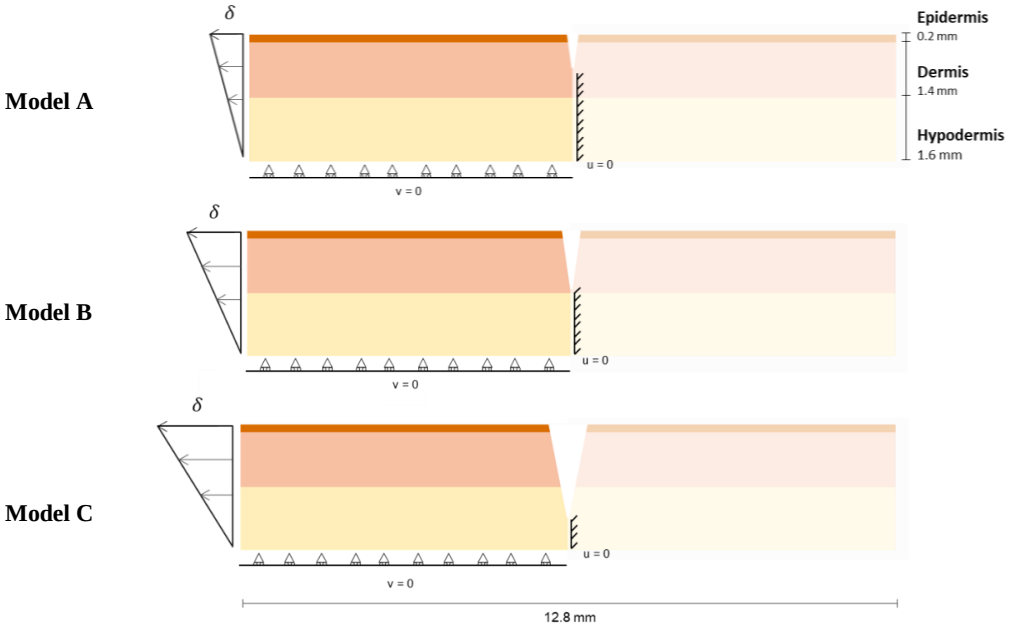

Fig. 1 - Model geometry and boundary conditions for model A, model B and model C.

Table 1 - Model dimensions and material properties.

Skin layer	Thickness - mm	Elastic Modulus (E) - MPa	Poisson's coefficient (ν)
Epidermis	0.2	102	0.48
Dermis	1.4	10.2	0.48
Hypodermis	1.6	0.0102	0.48

5. Results

The results obtained for the von Mises stress for model A, in which the wound is located entirely in the dermis, are presented in Fig. 2. Analysing the von Mises stress isomaps (Fig. 2(a)) it is possible to observe that the highest stress levels occurs in the end of the wound, in FEM and RPIM. The measurement of this parameter in specific points in the continuum of the wound (Fig. 2(b)) confirms the highest values of stress, around 1 MPa, in the end of the wound, in FEM and RPIM analysis.

The results obtained for the equivalent strain for the same model are presented in Fig. 3. Analysing the strain isomaps (Fig. 3(a)) it is possible to observe that the highest strain levels occurs in the hypodermis, in the two advanced discretization techniques used. The measurement of this parameter in specific points in the continuum of the wound (Fig.

3(b)) confirms the highest values of strain, around 0.12, in hypodermis, in FEM and RPIM. Moreover, it is possible to verify that the strain also increased in the end of the wound (around 0.04), in both FEM and RPIM methods (Fig. 3(b)).

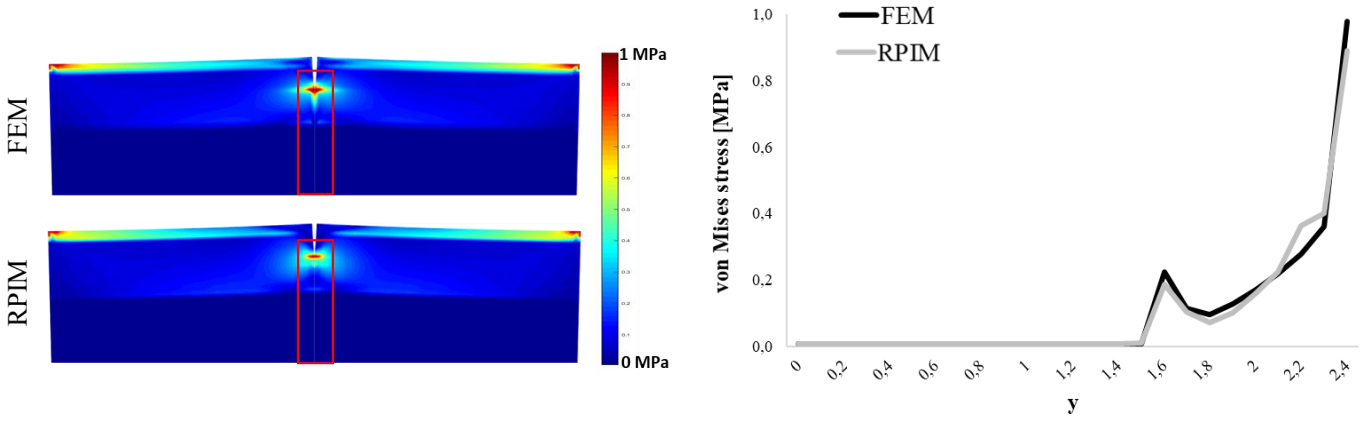

(a) (b)

Fig. 2 - (a) von Mises stress isomaps obtained with FEM and RPIM for model A; (b) von Mises stress measured in specific points in the area marked with the rectangle in the images, in the two advanced discretization techniques.

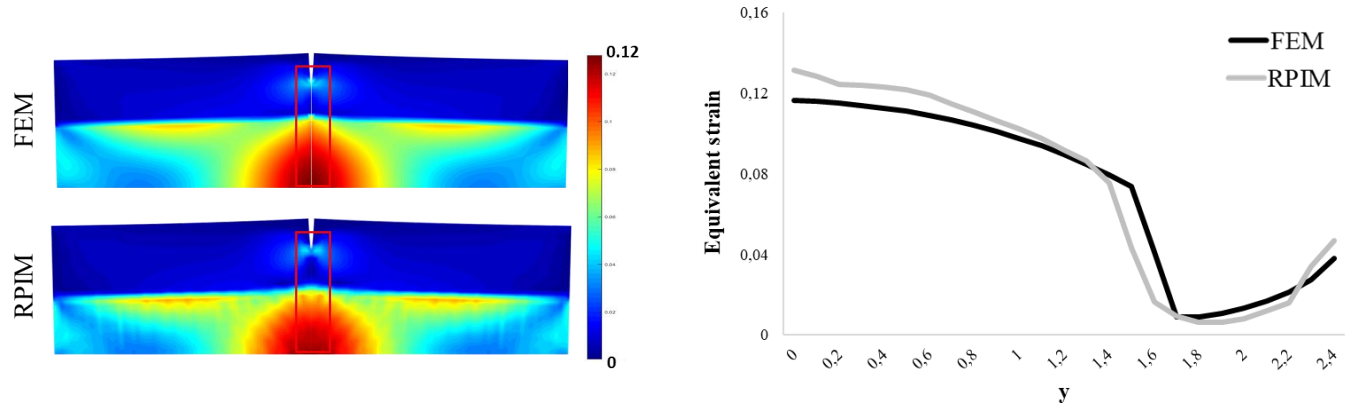

(a) (b)

Fig. 3 - (a) Equivalent strain isomaps obtained with FEM and RPIM for model A; (b) Equivalent strain measured in specific points in the area marked with the rectangle in the images, in the two advanced discretization techniques.

The results obtained for the von Mises stress for model B, in which the wound is located in the transition from the dermis to the hypodermis, are presented in Fig. 4. Analyzing the von Mises stress isomaps (Fig. 4(a)) it is possible to observe that the stress levels in the hypodermis are very low and homogenous, in FEM and RPIM analysis. In the end of the wound, it was observed a slight increase in the stress levels, mainly in RPIM analysis. The measurement of this parameter in specific points in the continuum of the wound (Fig. 4(b)) confirms the low (around 0.01 MPa) and homogeneous levels of stress in hypodermis, in the two discretization techniques.

The results obtained for the equivalent strain for the same model are presented in Fig. 5. Analysing the equivalent strain isomaps (Fig. 5(a)) it is possible to observe that the highest strain levels occurs in the hypodermis, in FEM and RPIM analysis. The measurement of these parameters in specific points in the continuum of the wound (Fig. 5(b)) confirms the highest values of strain, around 0.25, in hypodermis, in the two discretization techniques used.

The results obtained for the von Mises stress for model C, in which the wound is located until the hypodermis, are presented in Fig. 6. Analysing the von Mises stress isomaps (Fig. 6(a)) it is possible to observe that, analogous to the previous results, the stress levels in the hypodermis were very low and homogenous, in two advanced discretization techniques. The measurement of these parameters in specific points in the continuum of the wound (Fig. 6(b)) confirms the low (around 0.01 MPa) and homogeneous levels of stress in hypodermis, in FEM and RPIM analysis. In the end of the wound, it was observed a slight increase in the stress levels, around 0.02 MPa, in the two advanced discretization techniques used.

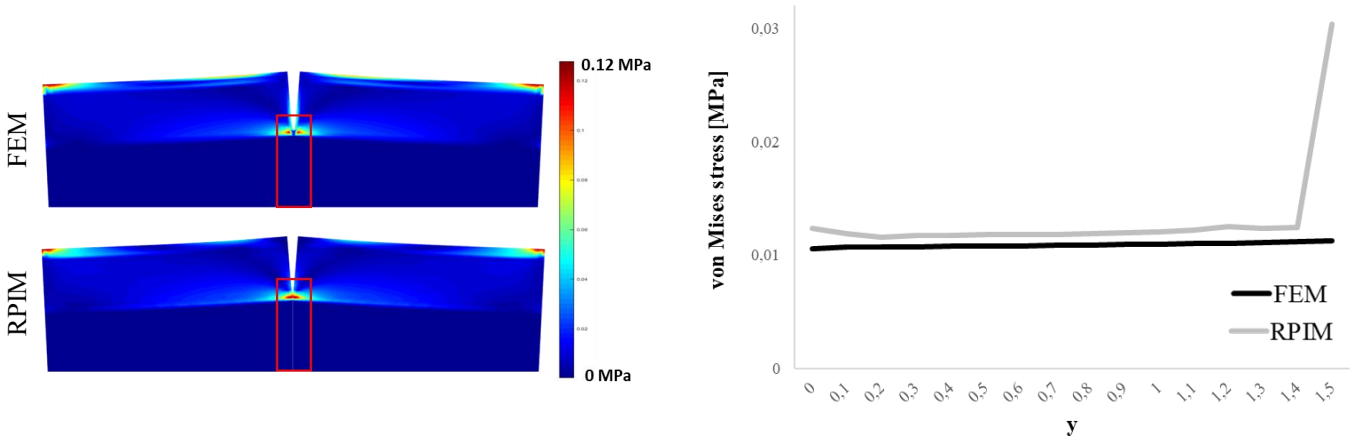

(a) (b)

Fig. 4 - (a) von Mises stress isomaps obtained with FEM and RPIM for model B; (b) von Mises stress measured in specific points in the area marked with the rectangle in the images, in the two advanced discretization techniques.

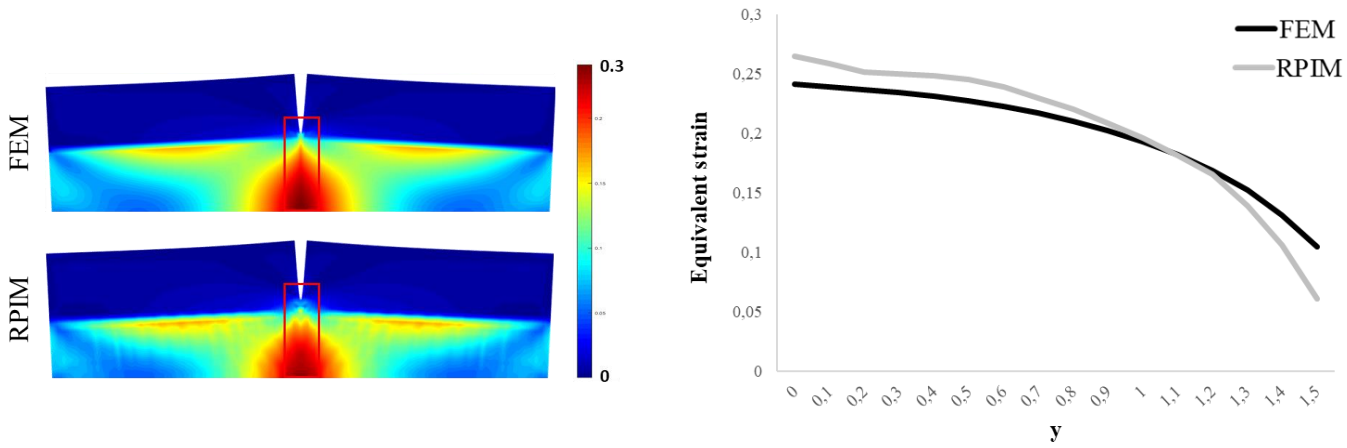

(a) (b)

Fig. 5 - (a) Equivalent strain isomaps obtained with FEM and RPIM for model B; (b) Equivalent strain measured in specific points in the area marked with the rectangle in the images, in the two advanced discretization techniques.

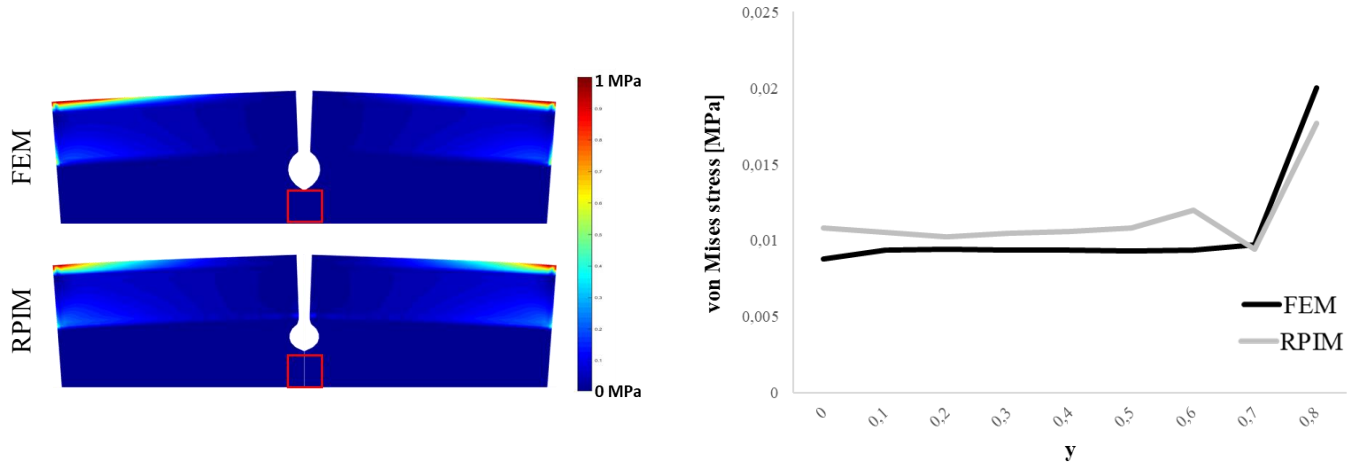

(a) (b)

Fig. 6 - (a) von Mises stress isomaps obtained with FEM and RPIM for model C; (b) von Mises stress measured in specific points in the area marked with the rectangle in the images, in the two advanced discretization techniques.

The results obtained for the equivalent strain for the same model are presented in Fig. 7. Analysing the equivalent strain isomaps (Fig. 7(a)) it is possible to observe that the highest strain levels occurred in the area around the wound, in the two advanced discretization techniques used. The measurement of these parameters in specific points in the continuum of the wound (Fig. 7(b)) confirms the highest values of strain, around 0.5, in the area around the wound, in FEM and RPIM analysis.

6. Discussion

Computational modelling is a very useful tool to predict stress profiles around the skin wounds, especially because there no exist methodologies to measure stress *in vivo* [14]. In this work, FEM and RPIM analysis were used to study the stress and strain fields in wounds with different depths. In our model, the highest levels of stress were obtained in the end of the wound, in both used techniques. Model A presented the highest stress levels, in both FEM and RPIM analysis. In Model B and C, where the wound was located in the hypodermis, the stress fields obtained presented smaller values. Regarding the strain fields, hypodermis presented the highest values, in FEM and RPIM analysis. These observations may be due to the mechanical properties of each skin layer. Hypodermis presents a low elasticity modulus, comparatively to dermis and epidermis, being more easily deformed. Indeed, this skin layer is mainly composed by adipose tissue, being a very soft tissue. Buganza Tepole and co-workers demonstrated the potential of FEM to analyse the stress profile in skin flap designs [15]. The authors analysed the von Mises stress concentration in different flap design and concluded that the maximum stress were located at the distal and proximal edges of the flap, and the obtained von Mises stress varied between 0 and 1.50 MPa.

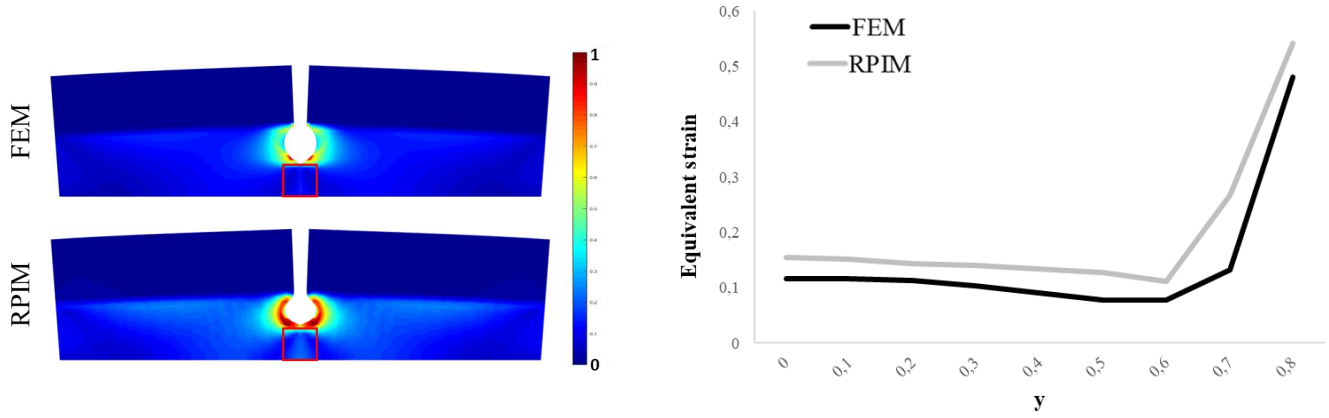

(a) (b)

Fig. 7 - (a) Equivalent strain isomaps obtained with FEM and RPIM for model C; (b) Equivalent strain measured in specific points in the area marked with the rectangle in the images, in the two advanced discretization techniques.

Human skin exhibits nonlinear stress-strain, anisotropic and viscoelastic characteristics [16]. Nevertheless, in order to decrease the model's complexity, most of the studies assume skin as an isotropic and linear elastic material [17]. Accordingly, in this study the skin was modelled as an isotropic and linear elastic material.

Although this is a preliminary study to assess the performance of these numerical methods in the analysis of stress profile in human skin it was possible to conclude that FEM and RPIM are valid numerical tools. The numerical methods used in the simulations demonstrated equivalent results. Moreover, the materials used in the simulations were well characterized in terms of elasticity. This kind of studies can be very useful in order to achieve new approaches and methodologies to improve wound healing.

Acknowledgements and Funding

The authors truly acknowledge the funding provided by Ministério da Ciência, Tecnologia e Ensino Superior - Fundação para a Ciência e a Tecnologia (Portugal), under Grant SFRH/BD/133894/2017. Additionally, the authors acknowledge the funding provided by LAETA, under project UIDB/50022/2020.

References

[1] Sen CK, Gordillo GM, Roy S, Kirsner R, Lambert L, Hunt TK, et al. Human skin wounds: a major and snowballing threat to public health and the economy. Wound Repair Regen. 2009;17(6):763-71.

[2] Posnett J, Franks PJ. The burden of chronic wounds in the UK. Nurs Times. 2008;104(3):44-5.

[3] Reihsner R, Balogh B, Menzel EJ. Two-dimensional elastic properties of human skin in terms of an incremental model at the in vivo configuration. Med Eng Phys. 1995;17(4):304-13.
[4] Singer AJ, Clark RA. Cutaneous wound healing. N Engl J Med. 1999;341(10):738-46.
[5] Wang P, Becker AA, Jones IA, Glover AT, Benford SD, Greenhalgh CM, et al. Virtual reality simulation of surgery with haptic feedback based on the boundary element method. Computers & Structures. 2007;85(7):331-9.
[6] Yang C, Tang D, Haber I, Geva T, del Nido PJ. In vivo MRI-based 3D FSI RV/LV models for human right ventricle and patch design for potential computer-aided surgery optimization. Computers & Structures. 2007;85(11):988-97.
[7] Flynn C. Finite element models of wound closure. J Tissue Viability. 2010;19(4):137-49.
[8] Lott-Crumpler DA, Chaudhry HR. Optimal patterns for suturing wounds of complex shapes to foster healing. J Biomech. 2001;34(1):51-8.
[9] Toutain CE, Brouchet L, Raymond-Letron I, Vicendo P, Bergès H, Favre J, et al. Prevention of Skin Flap Necrosis by Estradiol Involves Reperfusion of a Protected Vascular Network. Circulation Research. 2009;104(2):245-54.
[10] Whitcher FD. Simulation of in vivo loading conditions of nitinol vascular stent structures. Computers & Structures. 1997;64(5):1005-11.
[11] Fish J, Belytschko T. A First Course in Finite Elements: John Wiley & Sons; 2007.
[12] Belinha J. Meshless Methods in Biomechanics - Bone Tissue Remodelling Analysis: Springer International Publishing; 2014.
[13] Belytschko T, Krongauz Y, Organ D, Fleming M, Krysl P. Meshless methods: An overview and recent developments. Computer Methods in Applied Mechanics and Engineering. 1996;139(1-4):3-47.
[14] Cerda E. Mechanics of scars. Journal of Biomechanics. 2005;38(8):1598-603.
[15] Tepole AB, Gosain AK, Kuhl E. Computational modeling of skin: Using stress profiles as predictor for tissue necrosis in reconstructive surgery. Computers & structures. 2014;143:32-9.
[16] Silver FH, Freeman JW, DeVore D. Viscoelastic properties of human skin and processed dermis. Skin Res Technol. 2001;7(1):18-23.
[17] Zahouani H, Pailler-Mattei C, Sohm B, Vargiolu R, Cenizo V, Debret R. Characterization of the mechanical properties of a dermal equivalent compared with human skin in vivo by indentation and static friction tests. Skin Res Technol. 2009;15(1):68-76.

Journal of Computation and Artificial Intelligence in Mechanics and Biomechanics ISSN 2184-8971
Volume 1, Issue 2, Page 36-41, 2021

Estimating active forearm pronation-supination motion by means of FE modelling

Sánchez-Arce, I. J.[1]

[1] *Instituto de Ciência e Innovação em Engenharia Mecânica e Engenharia Industrial (INEGI); Rua Dr Roberto Frias 400, Campus da FEUP;4200-465; Porto;Portugal*

Abstract
Active range of motion (ROM) of the forearm is important for completing daily life activities (ADL). Such motion could be compromised as a result of a poorly healed fracture. Although numerical models are often used to aide medical treatment, most of them are static. In addition, there is no previous model nor methodology related to forearm and its motion. In this work, a methodology to create finite element models that can evaluate active ROM is developed and validated. The biomechanical behaviour of the ligamentous structures, as a whole, was compared with data available from previous studies. The active ROM was validated against experimental measurements of active ROM. The ROM predicted with this methodology was 72º in pronation and 83º in supination; these values are within 5º from the standardised values for human ROM. In addition, this work supports the hypothesis that the muscles are limiting structures of the ROM, such task was always attributed to ligamentous structures. Nevertheless, in active ROM, muscle contraction and extension delimited the arc of motion. In summary, this work provides a methodology, mechanical properties of ligamentous structures, types of constrains and kinematic assumptions to produce a biomechanically sound model of the forearm which can be used for further study of forearm fractures.

***DOI**: 10.5281/zenodo.4837374*

Article Info

Keywords
Finite element method
Human forearm models
Pronation-supination motion
Connector elements
Active forearm motion

Article History
Received: 29/10/2020
Revised: 01/02/2021
Accepted: 26/03/2021

1 Introduction

Forearm rotational motion is necessary for performing daily life activities (ADL) [1], [2]. It is known that malunion of forearm fractures can produce changes in forearm rotational range of motion (ROM), commonly reducing it [3]–[5]. The distal radius fracture (DRF) is the most common frequent. It has also been hypothesised that malunited DRFs could produce changes in the force transmitted in the distal radioulnar joint (DRUJ) [6].

Finite element modelling (FEM) has been used to analyse: a) the force transmitted at the DRUJ [7], and b) the effects of malunited forearm fractures [8]–[10]. However, no evidence of previous models that consider the bone motion or static models of the whole forearm has been found in the literature. Therefore, a complete methodology which takes into account the soft tissue structures involved in the pronation-supination (P-S) motion and their mechanical properties has to be developed. Also, models of the full forearm are necessary for this, which are also rare in the literature.

This paper aims to establish a methodology to develop FE models of the forearm that allow estimating P-S motion. Therefore, bone geometries form two forearms were extracted from computed tomography (CT) scans. Soft tissues involved in the P-S motion were identified and their mechanical properties were obtained from the literature. Once the proposed methodology is validated, it can be applied to modelling bones with malunited fractures for further studies, for example, changes in the ROM.

2 Methodology

2.1. Bone and cartilage geometries

Forearm geometry was extracted from computed tomography (CT) scans provided by the Wrightington Hospital. Image size was 512 x 512 pixels, the slice size was 500 μm. The left forearm corresponds to a 27-year-old male, the right to a 37-year-old female. The CT scans were segmented using ScanIP software (ScanIP 3.2, Simpleware LTD) following the procedure described in [11], [12]. Both cortical and trabecular bone layers were segmented separately, resulting in a more accurate bone representation. The bone geometry was exported as 'point cloud'; later, it was converted to solid geometry using SolidWorks (SolidWorks 2012, Dassault Systèmes). Finally, the solid models were imported into Abaqus (Abaqus 6.12, Dassault Systèmes).

Corresponding Author:
I.J. Sánchez-Arce
isidrodjsa@gmail.com

Cartilages were created in ScanIP by expanding the cortical bone surfaces. Cartilage thickness was considered constant and was determined as half of the minimum distance between articular surfaces. Afterwards, cartilage profiles were trimmed following anatomic descriptions, i.e., [13]. The cartilages correspond to the DRUJ and the proximal radioulnar joint (PRUJ). Finally, cortical and trabecular bone layers, as well as cartilages, were joint in Abaqus through Boolean operations.

2.2. Ligamentous structures and muscles

Two ligamentous structures stabilise the forearm motion, the distal radioulnar ligaments (DRUL) and the interosseous membrane (IOM). The DRUL connect the distal portions of the ulna and radius. The IOM connects the radius to the ulna along their shafts. The DRUL stabilises the pronation-supination motion. Although the IOM also stabilises the motion, its main function is to transmit load from the radius to the ulna. The IOM is composed of five regions, from which locations related to bone length can be calculated following the suggestions and proportions given by Noda et. al., [14]. A 'reference point'(RP) was positioned at the corresponding location; later, each RP was attached to a surface area, as anatomically as possible, through a 'kinematic coupling'; this process allowed to reduce stress concentration in attachment points. Afterwards, a spring element was placed between the anatomical locations, as shown in Figure 1a. All the springs were considered as tension-only and their stiffness was calculated as a function of their anatomical cross-sectional areas, which were reported by [14]–[16]; for the 'Distal accessory band' no area was found; however, in a later study Werner reported its stiffness [16]. The data was validated using areas and stiffness values from [14], [15]. The stiffness of each region is reported in Table **1**. Similarly, for the DRUL, their stiffness was calculated from the work of Schuind et. al., [17]; however, unlike them, in this work, both upper and lower DRUL regions were considered, as shown in Figure 1c. The DRUL mechanical stiffness values are listed in Table 2.

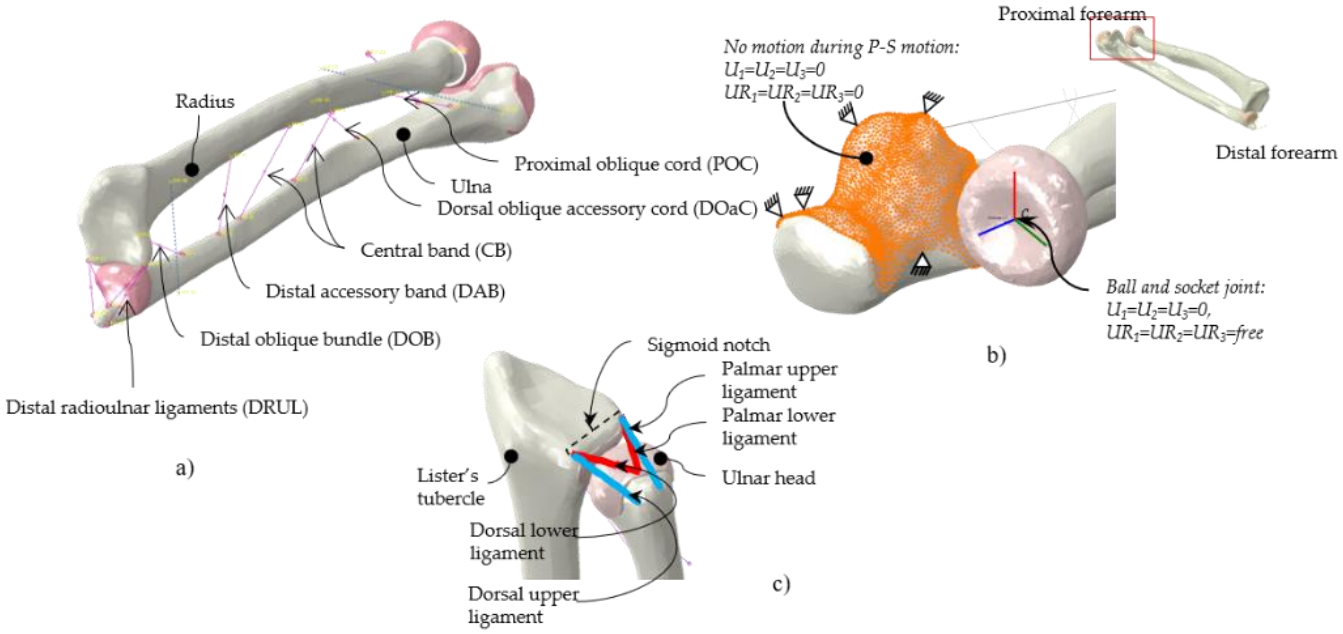

Figure 1. Interosseous membrane locations a), boundary conditions at the ulnar trochlea and radial head b), and the distal radioulnar ligaments c).

Table 1. Cross-sectional areas [14], and calculated individual stiffness for each IOM region.

IOM region	Cross-section area *(mm²)*	Stiffness *(N/mm)*
Central band (CB) (2 bundles)	12.61	103.24
Distal accessory band (DAB) [16]	--	11.2
Dorsal oblique bundle (DOB)	6.6	54.04
Proximal oblique cord (POC)	4.07	33.32
Dorsal oblique accessory cord (DOaC)	2.88	23.58

Subsequently, the biomechanical behaviour of the assembly was verified by numerically reproducing the experimental work performed by Hotchkiss et. al., [18], a good agreement was found. Although, the PRUJ anatomically possesses a complex arrangement of ligaments it also behaves kinematically as a ball and socket joint [7]. Consequently, this behaviour was represented by placing a connector element (CONN3D2) at the centre of the

radial head, and kinematically coupled to it. The connector element was configured to behave as a ball and socket joint (Figure 1b). Finally, the ulnar trochlea was fixed, as shown in Figure 1b.

On the other hand, it has been hypothesised that muscles cannot extend or contract beyond their anatomical limits, and so they can behave as a mechanical stop [19], [20]. Consequently, these structures could be used to determine the theoretical range of motion after a malunited fracture is present. Similarly, as it was done with the IOM and DRUL, the attachment points for the prime forearm movers were created and kinematically coupled to the bone surfaces (Figure 2) following the anatomical locations described by [13], [21], [22]. The prime movers are the pronator quadratus (PQ), pronator teres (PT), and the supinator muscle (Sup). These muscles were also simulated with a connector element configured as a tension-only spring in parallel to a contractile element, like Hill's muscle model. Therefore, active pronation-supination was achieved. The spring part of each connector was used as antagonist element. The antagonist force was determined from the measured change on length of each connector element and the electromyographic force reported by Gonzalez et. al., [23] during the pronation-supination motion. The resulting stiffness for each connector were: PQ=19.3 N/mm, PT=35.1 N/mm, and Sup=8.4 N/mm. Finally, the length of each connector representing a muscle was recorded, which will be used for further study of ROM reduction.

Table 2. Stiffness of each DRUL, values based on [17].

Ligament	Stiffness (*N/mm*)
Upper dorsal	6.6
Lower dorsal	6.6
Upper palmar	5.5
Lower palmar	5.5

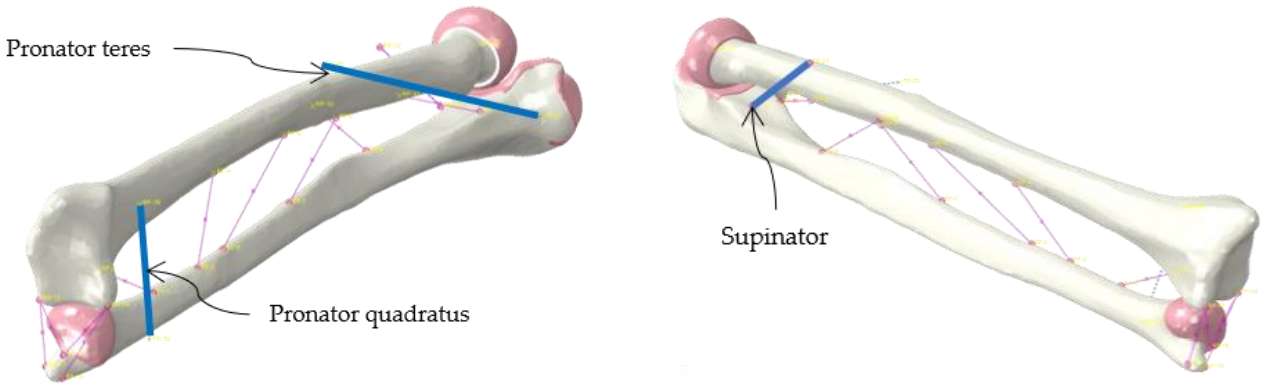

Figure 2. Forearm's prime movers simulated as connector elements.

ROM achieved was calculated from the initial and final coordinates of a few bony landmarks: ulnar and radial styloid processes, and the midpoint of the sigmoid notch, as shown in Figure 3. Once the simulation was completed, the coordinates of each point, throughout the full simulation, were exported as a spreadsheet (XSLX file).

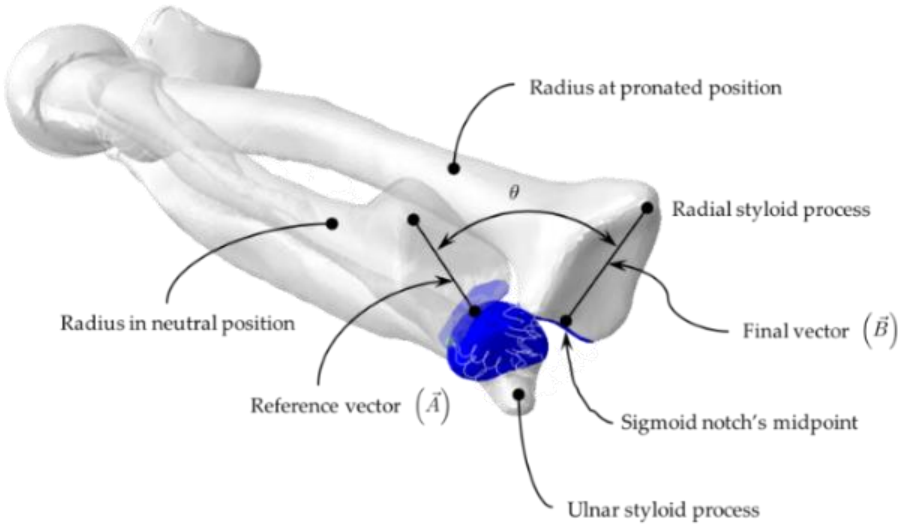

Figure 3 Anatomic bony landmarks for determining the model's ROM.

The ROM was calculated by means of the dot product between $\vec{A}$ and $\vec{B}$ (Figure 3). The angle was then calculated.

2.3. Mechanical properties, meshing and loading

Bone and cartilage were considered as linear-elastic materials because, at this stage, the models are focused on estimating ROM. The mechanical properties of bone and cartilage were taken from previous modelling of the wrist [8], [24], and are listed in Table 3.

Table 3. Mechanical properties of bone layers and cartilage used in the FE models.

Layer	Young's modulus (*MPa*)	Poisson's ratio
Cortical bone [24]	18000	0.20
Trabecular bone [24]	100	0.25
Cartilage [8]	10	0.30

The models were meshed using four-node tetrahedral elements (Abaqus C3D4). Element size varied according to the geometric regions of each bone. Element size was minimum in cartilaginous areas, muscle and ligament attachment regions, and areas where the cortical bone was thin, e.g., sigmoid notch area and ulnar trochlea. The number of nodes and elements were 112519 and 550255, respectively for the left model. The right model had 110056 nodes and 557555 elements.

Active motion was achieved by applying a negative displacement (contraction) to the connector elements representing the PQ and the Sup. Pronation was produced by applying -15.5 mm to the left PQ and -11.4 mm to the right PQ. Similarly, supination was produced by a -16.2 mm in the left model and -12.0 mm to the right model. The displacement applied to each connector was determined from previous testing of the model, as it was done for their antagonistic forces; in this case, to the range prior dislocation of the DRUJ. This had to be performed because the muscle length depends on the person's morphology; moreover, little information is available regarding these lengths, and so when morphologic specific data is required, it has to be extracted from medical images. However, no more data was available from the subjects who provided the CT scans.

3 Results

3.1. Range of motion

The left forearm model achieved a ROM of 71.4° and 82.4° for pronation and supination, respectively. The right forearm model reached 73.2° and 83.5°, respectively. These values are reported in Figure 4. These values were also compared with the 'anatomical' ROM described by the American Academy of Orthopaedic Surgeons (AAOS) [25] and with experimental measurements of active ROM from a control group (CG) composed of healthy individuals [26]. A difference of less than 3% was found (range 0.5% to 3%) with the data reported by the AAOS. On the other hand, a difference of less than 5% (range 3% to 4.4%) with the experimental data was observed.

3.2. Muscle lengths

As the models reached an active ROM consistent to anatomical measurements; in addition, it has been hypothesised that the muscle length also act as a limiting factor to the ROM [19], [20]. Consequently, the maximum and minimum length of each simulated muscle was recorded and reported in Table 4. Thus, these lengths would be used as constrains within the connector element configuration for further studies using these FEM and their variants.

Table 4. Maximum and minimum lengths of the simulated muscles.

	Length (mm)			
	Left		Right	
Muscle	Maximum	Minimum	Maximum	Minimum
Pronator quadratus	45.3	24.0	37.8	25.3
Pronator teres	102.5	87.8	96.4	85.6
Supinator	37.6	16.8	30.8	20.5

4 Discussion and conclusion

The main objective of these models was to simulate ROM; nevertheless, the geometry was created as accurate as possible, which increase the capability of the models for future analyses of stress and strain distributions in the bone surface. In this work, the IOM was represented with springs, one spring for each IOM region. Although stiffness of each region was theoretically calculated from a series of cadaveric studies, the agreement of the full assembly with another cadaveric study indicates that the proposed representation and stiffness of the IOM is anatomically representative.

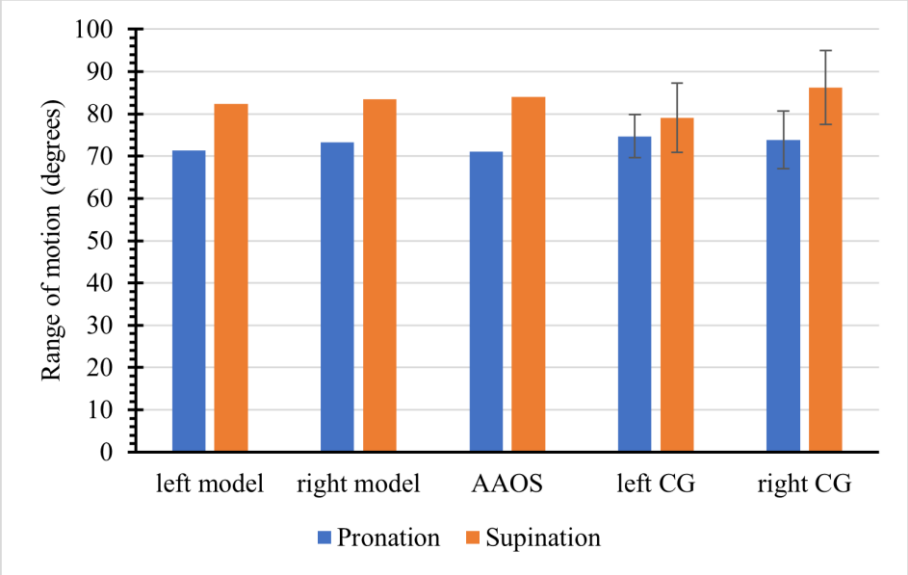

Figure 4. Comparison between the ROM obtained from the FEM models, and those from the American Academy of Orthopaedic Surgeons (AAOS), and from a Control Group (CG) texted experimentally by the author [26].

The assumption of considering the PRUJ as a ball and socket joint agreed with the kinematic models of forearm motion [27]. The chosen boundary conditions represent this ball and socket behaviour. This behaviour has been recently represented in other FE studies [23,24], in which the boundary conditions corresponding to the radial head are equal to those proposed here; however, those models did not investigate the forearm ROM. The motion was produced by the contraction of linear elements (connectors) and no motion axes were defined; thus, the radius rotates freely upon the ulnar surface. This is an advantage because geometrical changes are a consequence of a distal radius malunion, which also changes the position of the muscle attachment points. A similar concept was found in the literature, they were using springs to produce the motion [28], but antagonistic effects were not considered, whilst in this project both agonist and antagonist effects of the muscles were considered.

The achieved ROMs are close to the 'normal' ROM suggested by the AAOS [25]. The variation between the recommended and the achieved ROM is less than 10°, which according to clinical practice can be considered as a good agreement [29]. Similarly, the achieved ROM from the models are within the limits of an in-vivo study performed in healthy volunteers [26], with a difference of less than 5°. It was decided to use the recommended ROM because of the anatomic differences between the models; moreover, motion and morphology differences also exist amongst the volunteers conforming the experimental studies (e.g., CG and literature). In consequence, using a 'normal ROM' allow the results extracted from these models to be in a similar range to those available from other sources.

The use of connector elements for simulating the forearm active muscles provided a good alternative to simulate active forearm motion; moreover, the length of these elements (Table 4) provided to be a method for limiting the ROM in the models. This complies with the hypothesis of the muscles as limiting factors proposed by [19], [20]. Although that the muscle length has been anatomically considered as a limiting factor to the ROM, no evidence of its use in previous modelling work has been found. This approach, however, does not consider the wrapping of the muscle over the bone surfaces, which applies the force tangent to the surface. The use of banded ligamentous structures created from 'magnetic resonance images' (MRI) has been proposed by Gislason [12]; however, it was applied to a static model; in addition, it would require even more computational power because of the number of elements and the amount of contact interactions required. In addition, to the author's knowledge this is the first numerical model evaluating active forearm motion. Moreover, this work has also proved that the muscles had an effect in limiting the forearm motion, such effect was often attributed to ligamentous structures.

In conclusion, the methodology briefly described in this work can produce biomechanically sound FE models that can be used for studying limb rotational motion, like the forearm pronation-supination. Moreover, the calculated stiffness values for each of the regions of the interosseous membrane is a secondary contribution that could benefit FE models, like those used to analyse load distribution for radial head prostheses.

Acknowledgements and Funding

The author thanks CONACyT (Consejo Nacional de Ciencia y Tecnología) Mexico for the scholarship that made possible this research. Moreover, thanks Prof Teresa Alonso and Dr Alan Walmsley for their advice during the development of this work. Finally, thanks to Prof Adam C Watts for the CT scans necessary to create the 3D models.

References

[1] B. F. Morrey, L. J. Askew, and E. Y. S. Chao, "A biomechanical study of normal functional elbow motion.," *J. Bone Joint Surg. Am.*, vol. 63, no. 6, pp. 872–7, Jul. 1981.
[2] M. Sardelli, R. Z. Tashjian, and B. A. MacWilliams, "Functional Elbow Range of Motion for Contemporary Tasks," *J. Bone Jt. Surg.*, vol. 93, no. 5, pp. 471–477, 2011.
[3] G. S. Fraser, L. M. Ferreira, J. A. Johnson, and G. J. W. King, "The Effect of Multiplanar Distal Radius Fractures on Forearm Rotation: In Vitro Biomechanical Study," *J. Hand Surg. Am.*, vol. 34, no. 5, pp. 838–848, 2009.
[4] H. Hirahara, P. G. Neale, Y.-T. Lin, W. P. Cooney, and K.-N. An, "Kinematic and torque-related effects of dorsally angulated distal radius fractures and the distal radial ulnar joint," *J. Hand Surg. Am.*, vol. 28, no. 4, pp. 614–621, 2003.
[5] L. M. Ferreira, G. S. Greeley, J. A. Johnson, and G. J. W. King, "Load transfer at the distal ulna following simulated distal radius fracture malalignment.," *J. Hand Surg. Am.*, vol. 40, no. 2, pp. 217–23, Feb. 2015.
[6] B. D. Adams, "Effects of radial deformity on distal radioulnar joint mechanics," *J. Hand Surg. Am.*, vol. 18, no. 3, pp. 492–498, 1993.
[7] D. Greybe, M. R. Boland, T. Wu, and K. Mithraratne, "A finite element model to investigate the effect of ulnar variance on distal radioulnar joint mechanics.," *Int. j. numer. method. biomed. eng.*, Mar. 2016.
[8] D. D. Anderson, B. R. Deshpande, T. E. Daniel, and M. E. Baratz, "A three-dimensional finite element model of the radiocarpal joint," *Iowa Orthop. J.*, vol. 25, p. 10, 2005.
[9] J. Tan, M. Mu, G. Liao, Y. Zhao, and J. Li, "Biomechanical analysis of the annular ligament in Monteggia fractures using finite element models," *J. Orthop. Surg. Res.*, vol. 10, no. 1, p. 30, 2015.
[10] T. Miyake, H. Hashizume, H. Inoue, Q. Shi, and N. Nagayama, "Malunited Colles' fracture Analysis of stress distribution," *J. Hand Surg. Br. Eur. Vol.*, vol. 19, no. 6, pp. 737–742, 1994.
[11] Simpleware_LTD, "ScanIP, ScanFE and ScanCAD version 3.1; Tutorial guide." Simpleware LTD, 2008.
[12] M. K. Gíslason and D. H. Nash, "Finite element modelling of a multi-bone joint: the human wrist," in *Finite Element Analysis - New Trends and Developments*, F. Ebrahimi, Ed. InTech, 2012.
[13] N. Palastanga, R. Soames, and D. Field, *Anatomy and human movement: structure and function*, 4th ed. Edinburgh: Butterworth-Heinemann, 2002.
[14] K. Noda, A. Goto, T. Murase, K. Sugamoto, H. Yoshikawa, and H. Moritomo, "Interosseous Membrane of the Forearm: An Anatomical Study of Ligament Attachment Locations," *J. Hand Surg. Am.*, vol. 34, no. 3, pp. 415–422, 2009.
[15] H. J. Pfaeffle *et al.*, "Tensile properties of the interosseous membrane of the human forearm," *J. Orthop. Res.*, vol. 14, no. 5, pp. 842–845, 1996.
[16] F. W. Werner, J. L. Taormina, L. G. Sutton, and B. J. Harley, "Structural properties of 6 forearm ligaments.," *J. Hand Surg. Am.*, vol. 36, no. 12, pp. 1981–7, Dec. 2011.
[17] F. Schuind *et al.*, "The distal radioulnar ligaments: A biomechanical study," *J. Hand Surg. Am.*, vol. 16, no. 6, pp. 1106–1114, 1991.
[18] R. N. Hotchkiss, K.-N. An, D. T. Sowa, S. Basta, and A. J. Weiland, "An anatomic and mechanical study of the interosseous membrane of the forearm: Pathomechanics of proximal migration of the radius," *J. Hand Surg. Am.*, vol. 14, no. 2, Part 1, pp. 256–261, 1989.
[19] M. S. Feeney, F. Wentorf, and M. D. Putnam, "Simulation of altered excursion of the pronator quadratus.," *J. Wrist Surg.*, vol. 3, no. 3, pp. 198–202, Aug. 2014.
[20] C. C. Norkin and D. J. White, *Measurement of joint motion: a guide to goniometry*, Fifth. F. A. Davis Company, 2016.
[21] C. Fontaine, F. Millot, D. Blancke, and H. Mestdagh, "Anatomic basis of pronator quadratus flap," *Surg. Radiol. Anat.*, vol. 14, no. 4, pp. 295–299, 1992.
[22] H. Gray, *Gray's Anatomy*, 35th editi. London: Longman Group LTD, 1973.
[23] R. V Gonzalez, E. L. Hutchins, R. E. Barr, and L. D. Abraham, "Development and evaluation of a musculoskeletal model of the elbow joint complex," *J. Biomech. Eng.*, vol. 118, no. 1, pp. 32–40, 1996.
[24] M. K. Gíslason, B. Stansfield, and D. H. Nash, "Finite element model creation and stability considerations of complex biological articulation: The human wrist joint," *Med. Eng. Phys.*, vol. 32, no. 5, pp. 523–531, 2010.
[25] D. C. Boone and S. P. Azen, "Normal range of motion of joints in male subjects.," *J. Bone Joint Surg. Am.*, vol. 61, no. 5, pp. 756–9, Jul. 1979.
[26] I. de J. Sánchez-Arce, A. Walmsley, M. Fahad, and E. S. Durazo-Romero, "Lateral differences of the forearm range of motion," *J. Eng. Med.*, vol. 234, no. 5, pp. 496–506, 2020.
[27] A. M. Weinberg, I. T. Pietsch, M. B. Helm, J. Hesselbach, and H. Tscherne, "A new kinematic model of pro- and supination of the human forearm," *J. Biomech.*, vol. 33, no. 4, pp. 487–491, 2000.
[28] S. Shimawaki, M. Ebe, M. Nakabayashi, and N. Sakai, "Simulation of the stabilizing mechanism of distal radioulnar joint during pronation and supination," *J. Biomed. Sci. Eng.*, vol. 8, no. 3, p. 15, 2013.
[29] A. D. Armstrong, J. C. MacDermid, S. Chinchalkar, R. S. Stevens, and G. J. W. King, "Reliability of range-of-motion measurement in the elbow and forearm.," *J. shoulder Elb. Surg.*, vol. 7, no. 6, pp. 573–580, 1998.

Journal of Computation and Artificial Intelligence in Mechanics and Biomechanics ISSN 2184-8971
Volume 1, Issue 2, Page 42-47, 2021

Influence of middle ear tumours on the biomechanical behaviour of the chorda tympani

Leonor Mendonça[1,3], Carla F. Santos[1,3], Fernanda Gentil[1,2], Marco Parente[1,3], Bruno Areias[1,3], Renato Natal Jorge [1,3]

[1] *INEGI, Institute of Mechanical Engineering and Industrial Management, Rua Dr. Roberto Frias, Porto, Portugal.*
[2] *Clínica ORL-Dr. Eurico Almeida, Widex, Escola Superior de Saúde – I.P.Porto, Porto,Portugal*
[3] *FEUP, Faculty of Engineering of the University of Porto, Rua Dr. Roberto Frias, Porto, Portugal*

Abstract
Chronic otitis media may lead to the development of a cholesteatoma, a benign middle ear tumour. If this occurs, the chorda tympani nerve, a facial nerve branch that crosses the middle ear, may be compromised. The influence of cholesteatoma development near chorda tympani nerve was studied, in order to assess the consequences of this mass in terms of possible facial paralysis. To do so, an ear model based on the finite element method was used. The chorda tympani nerve was originally discretized and assembled in the model. Two different sized tumours were created so cholesteatoma growth could be simulated. The pressure in this nerve were assessed in two moments - when the tumour first interacts with it, pushing it down, and when the tumour compresses it against the incus. Moreover, the effect of applying pressure directly on the nerve was also evaluated, so tumour geometry did not interfere in the analysis. The obtained stress allowed to infer on the consequences regarding taste disturbance and facial paralysis, although some studies report that when pressure fades away, it is possible to fully recover. The von Mises stress was higher when the chorda tympani nerve was pushed against the incus by the large tumour, in the contact area between the nerve and the ossicle.

***DOI**: 10.5281/zenodo.4843432*

Article Info

Keywords
Finite element method
Biomechanics
Chorda tympani nerve

Article History
Received: *29/10/2020*
Revised: *26/03/2021*
Accepted: *11/05/2021*

1. Introduction

Chorda tympani nerve (CTN) is a nerve that arises from the facial nerve and crosses the tympanic cavity between the malleus and the incus. The course of CTN can be divided into three portions, as it is shown in Fig. 1, connecting the facial to the lingual nerve [1, 2]. CTN provides parasympathetic innervation to submandibular and sublingual glands as well as special sensory taste fibres for the anterior two thirds of the tongue, through the lingual nerve, being this way related to saliva secretion and taste sensation [3, 4]. As there is no cover involving the CTN, this structure is highly vulnerable to the events that happen in its surroundings [5, 6].

Some studies to better understand the CTN have been conducted over time. CTN was described in literature as having a diameter between 0.3 and 0.5 mm, showing wide inter patient variation [7]. In order to have a better surgery outcome, Liu et al. studied the whole course of some deep nerves in human head [2]. Regarding CTN, the values for the part that crosses the tympanic cavity were a diameter around 0.44 mm and a length of 9.83 ± 1.24 mm.

Otitis media (OM) is a middle ear infection that can either occur as an acute otitis media or, if it lasts longer than three months, as a chronic otitis media (COM). The latter may lead to tumour development, being cholesteatoma the most common tumour that occurs as a consequence of a COM. Cholesteatomas are middle ear benign tumours, characterized for being pouch like lesions and resulting from accumulations of skin debris [8].Cholesteatomas may affect the surrounding structures as it grows, as it can trigger an inflammatory reaction, which leads to the appearance of osteoclasts, that are capable of destroying bone cells [9, 10], leading to ossicular chain erosion. Moreover, if the tumour grows in such a site that pressures the CTN, it can affect this nerve's function, which can ultimately result in facial palsy (FP), the inability to move a part of the face.

Publicações ISEP - https://publicacoes.isep.ipp.pt/jcaimb | ZENODO repository - https://zenodo.org/
Corresponding Author:
Carla Santos
fsantos.carla@gmail.com

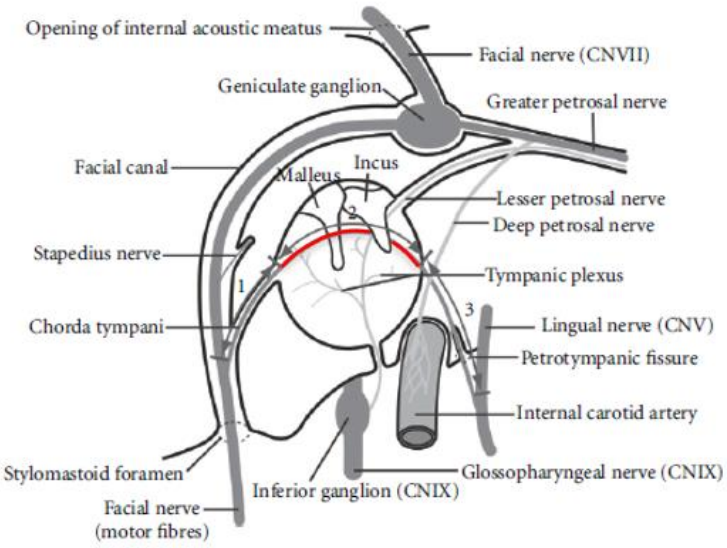

Fig. 1 - CTN portions between the facial nerve and the lingual nerve. Portion 1: mastoid process, portion 2: tympanic cavity, portion 3: submandibular fossa [2].

Former studies show that there is a close connection between pressure and the induction of osteoclastic bone resorption that is typically associated to cholesteatomas. Thus, Orisek and Chole conducted a research on the pressure exerted by cholesteatomas on nearby structures [11]. The results pointed to pressures between 1.31 and 11.88 mm Hg, equivalent to 174 and 1 584 Pa respectively, being the ones that lead to greater osteoclastic activity.

The link between FP and OM and cholesteatoma was also a matter of interest. Takahashi et al. (1985) conducted a study to assess this connection, concluding that FP caused by COM usually occurred together with cholesteatoma or acute increase of inflammation in the middle ear, being the paralysis mild and its progression slow. Savic and Djeric (1989) conducted a study including 1 261 patients that were subjected to a surgery due to COM. Of all these patients, 64 showed FP before surgical intervention, being a cholesteatoma present in 52 (80%) of these cases. This suggests that FP is highly connected to cholesteatoma following COM. After surgery, complete recovery was managed in 45 (70%) of the patients [12]. Thus, surgery can be considered an efficient approach to restore facial function. In 2001, Hu and Wang studied the connection between CTN and cholesteatoma development in its surroundings, concluding that cholesteatoma leads to ultrastructural changes of the CTN [13]. In 2007, Clark and O'Malley studied the influence of iatrogenic CTN injuries [14]. The results suggest that cholesteatoma leads to damages in CTN, as patients with cholesteatoma show less symptoms alteration after nerve injury during surgery, which indicates that the tumour leads to CTN hypofunctioning.

Patients that suffer from FP due to the pressure exerted by a cholesteatoma usually recover the facial functions after cholesteatoma removal, as the pressure on the nerve vanishes. The time period for this recovery can go up to some months. However, if for some reason the cholesteatoma causes irreparable damages in the nerve, facial function may never return to normal. The most critical period when referring to cholesteatoma recurrence are the first two years after surgery, as most reported cases happen during this term [9]. Recurrence of 26.9% was obtained in a study conducted by Syms and Luxford in 2003 [15]. Thus, the aim of this work was to evaluate the influence of cholesteatoma size in the CTN pressure, which could lead to FP.

2. Methods

The Finite Element Method was used as discretization technique in the current study, being FEMAP© and ABAQUS© the used software, the first used to model the cholesteatomas and the CTN and the latter to run the simulations [16]. Two different sized tumours were built and assembled to the middle ear model, in the connection between the malleus and the incus, as the development of a tumour in this location would affect CTN [17]. The geometries had an ellipsoid shape, considering that the smaller one should reach the CTN area only from above and the bigger one should be large enough to partially wrap the CTN, so the effects of the tumour compressing the nerve against the incus could be tested. According to Raveh Tilleman et al., that studied cancerous tissue mechanical properties, this tissue Poisson's ratio is 0.43±0.12 and the Young's modulus is, on average, 52 kPa [18]. Therefore, an elastic behaviour

considering these values was defined for the cholesteatomas. CTN was then modelled, improving the existing middle ear model. This structure was originally modelled in the present work and incorporated in the computational model.

According to the previously mentioned values obtained by Liu et al., and supported by the description of the nerve course, it was possible to create a reliable computational representation of the CTN [2]. The modelled CTN had the diameter reported by Liu et al., 0.44 mm, and its length was slightly higher, as the nerve had to be adjusted to the structures present in the used middle ear model, being its value 13.3 mm.

The mesh was created, being composed of 2875 nodes and 2052 C3D8 elements. Due to scarce information regarding CTN properties, the Poisson's coefficient and the Young's modulus assigned to this structure were based on a study regarding the mechanical properties of the sciatic nerve, conducted by Liu et al., being 0.37 and 4.1×10^7 N/m^2, respectively [19]. After modelling and meshing the CTN in the appropriate position, this structure was properly adjusted to the ossicles and the simulations were performed. The main goal was to understand the behaviour of the CTN when pressured by a cholesteatoma. Thus, the simulations were performed considering that the CTN would be initially pushed down and then, as the tumour grows, pushed against the incus. As the idea was to simulate the pressure exerted by the cholesteatoma growth, an internal pressure was defined to simulate it. Thus, a shell with the tumour shape was created and connected to the ossicles.

The first simulations were made with the smaller tumour, with an associated pressure of 174 Pa, corresponding to the lower value obtained by Orisek and Chole. This way, this pressure was applied in the internal surface of the shell [11]. The CTN was fixed in its extremities and the ossicles were totally immobilized. The part of the shell connected to the ossicles was also fixed. The von Mises stress was analysed in three different nodes of the CTN, as showed in Fig. 2. The chosen nodes were X, a central node in the part of the CTN that is pushed down in the first interaction between the CTN and the cholesteatoma, Y, a central node in the section of CTN that contacts with the incus, on the side on which the cholesteatoma would apply pressure, and Z, not visible in the representation, a central node in the part of the CTN that would be pressed against the incus, in the opposite side of Y.

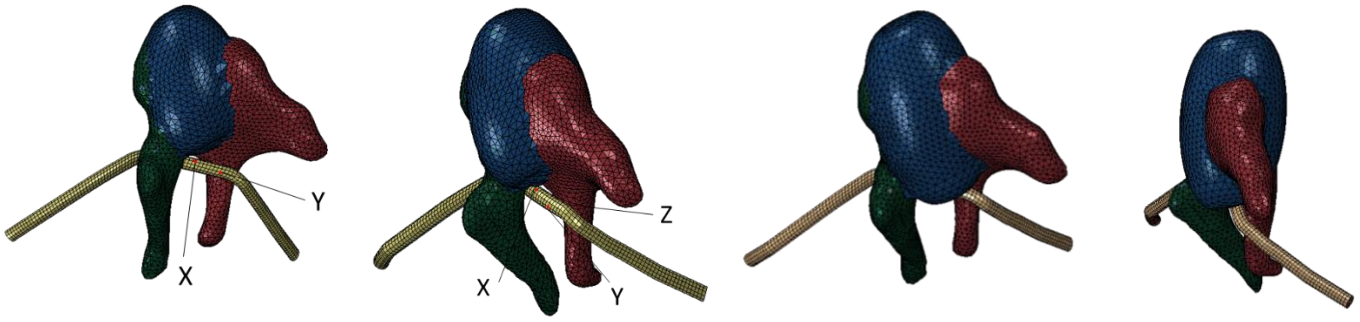

Fig. 2 - CTN (yellow) and small (left) and large (right) cholesteatomas (blue) in the middle ear. X, Y and Z are nodes in which the results of applying pressure on CTN were assessed. Green ossicle: malleus, red ossicle: incus.

Then, the interaction between the CTN and the large tumour was studied. The same procedure was applied for the large tumour. Instead of applying an internal pressure of 174 Pa, a higher value in the pressure interval described in the work of Orisek and Chole (174 – 1 584 Pa) was used. As it is a large tumour, but it can still grow and be capable of exerting higher pressures on the surrounding structures, the chosen value for this simulation was 1 300 Pa. The results were analysed in the same nodes. In order to better evaluate the effect of compressing CTN against the incus, an additional simulation was performed. This way, a pressure was applied directly in the CTN, in order to simulate the effect of the tumour. The used values of pressure were the same as in the previous simulations, 174 and 1 300 Pa, being the results analysed for the two nodes close to the incus, Y and Z.

3. Results

The von Mises stresses were analysed and compared for the three different mentioned locations. The influence of the tumours growth was analysed and then the effects of applying pressure directly on the CTN were also evaluated. Initially, this was tested by expanding the tumours towards the CTN. The effects of applying an internal pressure of 174 Pa on the small tumour shell were assessed. Table 1 shows the von Mises stress obtained for nodes X, Y and Z and Fig. 3 the stress distribution on CTN.

Table 1 – von Mises stress obtained for the CTN when affected by the cholesteatomas.

Nodes	X	Y	Z
von Mises stress for small tumor (Pa)	94699	217012	334652
von Mises stress for large tumor (Pa)	89064	181840	404098

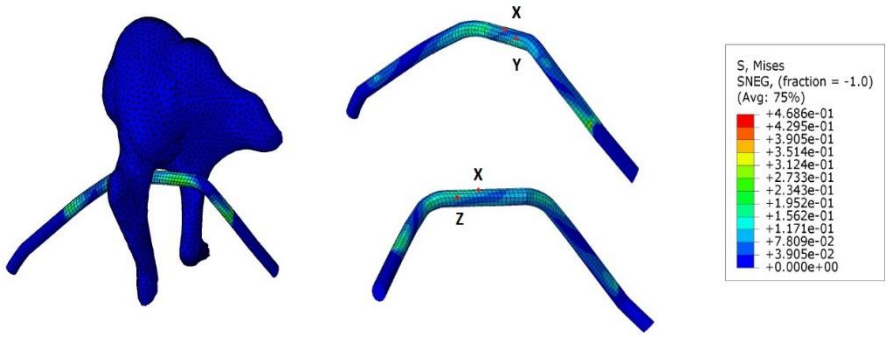

Fig. 3 – von Mises stress obtained for the CTN when affected by the small tumour.

The large tumour influence on CTN was then studied. Table 1 shows the von Mises stress obtained for the three nodes, for a pressure of 1 300 Pa. In Fig. 4 it is possible to observe the stress distribution on CTN.

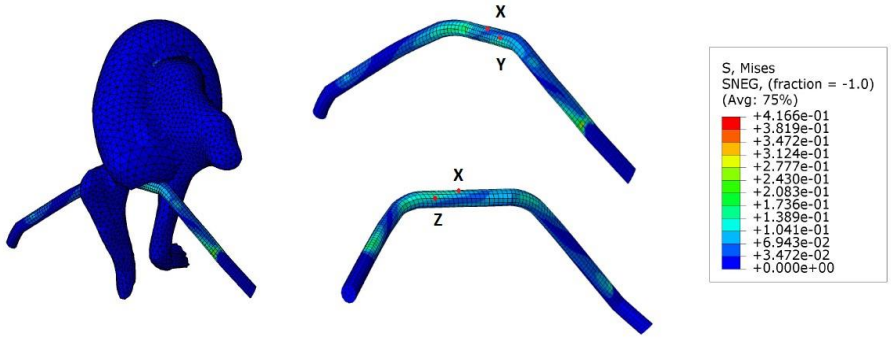

Fig. 4 – von Mises stress obtained for the CTN when affected by the large tumour.

Finally, the effect of applying a pressure directly on the CTN surface was studied, being the results in Table 2.

Table 2 – von Mises stress obtained for the CTN when pressure is directly applied on its surface.

Nodes	Y	Z
von Mises stress (Pa) for an applied pressure of 174 Pa	217017	337067
von Mises stress (Pa) for an applied pressure of 1300 Pa	217054	352899

4. Discussion

The hypothesis considered in the present work was the influence of cholesteatoma size in the CTN stress. The results showed that the cholesteatoma size seems to have influence in the CTN stress only when it contacts with a stiffer structure as the incus and couldn´t move.

In what concerns the simulations related to the small tumour, it is possible to observe that the higher stress value occurs for the node that contacts with the incus, Z. Although node X is closer to the pressure source, the cholesteatoma, this part of the CTN can move freely without any other structure blocking its movement. This way, the higher stresses will be related to the node that contacts with the incus, as this ossicle blocks CTN movement.

It is possible to observe that, regarding the large tumour, the highest stress value occurs, once again, for the node in contact with the incus. In general, it would be expected that the stress values concerning the large tumour were higher than the ones obtained for the smaller one, which does not happen. Nevertheless, it is important to take into consideration that the tumour shape may have influence. This way, and as the large tumor had to be adjusted to the CTN, its lower face is not flat as it is the one of the smaller tumour. The irregularity of the large tumour lower surface may be the reason why

the applied internal pressure does not lead to higher stresses. The differences in the cholesteatoma shape outline should be considered in a further research, as it could influence the results. However, the von Mises stress values obtained in the node Z, which is the node with the same conditions in both simulations (pressured against the incus) showed the higher difference between both tumours, with higher stress for the large tumour. This should be considered the most relevant analysis in the present work, as the FP has higher probability to occur when the CTN is pressured to a stiffer structure.

By applying pressure directly on the CTN, it is possible to observe that the stress is higher when a higher pressure is applied, being this difference more relevant in node Z, the node that contacts directly with the incus. This may be explained by the fact that this node has a fixed barrier to stop its movement, the incus, which causes a higher stress on the CTN.

It is possible to observe that node Z is the one with higher stress in all the performed simulations, which is expected as this is the node that contacts directly with the incus. For the simulations using the developed cholesteatomas, the stress associated to the large tumour was around 20% higher than the stress in the case where the small tumour effects were analysed.

As no former studies were found regarding this topic, it was not possible to compare these results with literature values. Thus, the obtained results only allow to infer on possible outcomes for CTN damage, as cholesteatoma continues to grow. As CTN crosses the middle ear close to the ossicles, tumour growth near this structure will probably permanently damage the CTN by compression against one of the ossicles, leading to higher stress in CTN. Being compressed by the cholesteatoma against the incus may lead to highly taste distortion and, eventually, FP, if the pressure on CTN is high. Nevertheless, several studies suggest that these symptoms are likely to disappear when pressure fades away. Furthermore, it was possible to conclude that a cholesteatoma that grows in the same site as the one simulated in this work starts to directly interfere with CTN from the moment it has a dimension slightly superior to the smaller tumour.

5. Conclusion

The results suggest that the fact that the CTN runs uncovered in the middle ear makes it more susceptible to be damaged by any unexpected body that can grow nearby.

Node Z is the one that records higher stresses in all cases, with an increase of around 20% for the larger tumour in the first simulations. The obtained stresses show that the fact that CTN is positioned between two ossicles, it increases the possibility of permanently damage by compression it against a fixed and stiffer structure. This allows taste disturbance and, possibly, facial paralysis.

Nomenclature	
CTN	*Chorda tympani nerve*
OM	*Otitis media*
COM	*Chronic otitis media*
FP	*Facial palsy*

Acknowledgements and Funding

The authors acknowledge the funding by "Ministério da Ciência, Tecnologia e Ensino Superior —Fundação para a Ciência e a Tecnologia , Portugal and POCH —Programa Operacional Capital Humano, comparticipado pelo Fundo Social Europeu e por fundos nacionais do MCTES" under research grants SFRH/BD/108292/2015 and by project funding MIT- EXPL/ISF/0084/2017. Additionally, the authors gratefully acknowledge the funding of Project NORTE-01-0145-FEDER-000022 —SciTech —Science and Technology for Competitive and Sustainable Industries, cofinanced by Programa Operacional Regional do Norte (NORTE2020), through Fundo Europeu de Desenvolvimento Regional (FEDER).

References

[1] Erlo Esslen. Investigations, part ii: Electrophysiologic investigations on the natural history of acute facial palsies. In *The Acute Facial Palsies*, pages 39–116. Springer, 1977.

[2] Longping Liu, Robin Arnold, and Marcus Robinson. Dissection and exposure of the whole course of deep nerves in human head specimens after decalcification. *International journal of otolaryngology*, 2012, 2012:418650.

[3] JVD Hough. Malformations and anatomical variations seen in the middle ear during the operation for mobilization of the stapes. *The Laryngoscope*, 68(8):1337–1379, 1958.

[4] B Minnigerode. Intratympanale aufzweigung der chorda tympani, eine seltene anatomische verlaufsvariante. *Acta Oto-Laryngologica*, 59(1):20–22, 1965.
[5] Orhan Gedikli, Harun Dogru, Gülsen Aydin, Mustafa Tüz, Kemal Uygur, and Aliye Sari.˘ Histopathological changes of chorda tympani in chronic otitis media. *The Laryngoscope*, 111(4):724–727, 2001.
[6] Katarina Berling, Paula Mannström, Mats Ulfendahl, Niklas Danckwardt Lilliestrom, and Magnus Von Unge. The chorda tympani degenerates during chronic otitis media: an electron microscopy study. *Acta Oto-Laryngologica*, 135(6):542–548, 2015.
[7] Jack H Noble, Frank M Warren, Robert F Labadie, and Benoit M Dawant. Automatic segmentation of the facial nerve and chorda tympani in ct images using spatially dependent feature values. *Medical physics*, 35(12):5375–5384, 2008.
[8] Minoru Ikeda, Hidehisa Nakazato, Keiko Onoda, Ryoji Hirai, and Akinori Kida. Facial nerve paralysis caused by middle ear cholesteatoma and effects of surgical intervention. *Acta otolaryngologica*, 126(1):95–100, 2006.
[9] LMJ Lips, PJ Nelemans, FMD Theunissen, E Roele, J van Tongeren, JR Hof, and AA Postma. The diagnostic accuracy of 1.5 t versus 3 t non-echo-planar diffusion-weighted imaging in the detection of residual or recurrent cholesteatoma in the middle ear and mastoid. *Journal of Neuroradiology*, 47(6):433-440, 2019.
[10] Kenneth L Kennedy and Achint K Singh. Middle ear cholesteatoma. In *StatPearls*. StatPearls Publishing, 2019.
[11] Brian S Orisek and Richard A Chole. Pressures exerted by experimental cholesteatomas. *Archives of Otolaryngology–Head & Neck Surgery*, 113(4):386–391, 1987.
[12] DRAGOSLAV LJ SAVIC and DRAGOSLAVA R DJERI´ C. Facial paralysis in chronic suppurative otitis media. *Clinical Otolaryngology & Allied Sciences*, 14(6):515–517, 1989.
[13] Z Hu and Z Wang. Research of the chorda tympani nerve in cholesteatoma. *Zhonghua er bi yan hou ke za zhi*, 36(2):123–125, 2001.
[14] Matthew PA Clark and Steve O'Malley. Chorda tympani nerve function after middle ear surgery. *Otology & Neurotology*, 28(3):335–340, 2007.
[15] Mark J Syms and William M Luxford. Management of cholesteatoma: status of the canal wall. *The Laryngoscope*, 113(3):443–448, 2003.
[16] *ABAQUS Analysis User's Manual*, 2019.
[17] Bruno André Faria Areias. Simulação biomecânica do ouvido humano, incluindo patologias do ouvido médio. *Master Thesis. Porto, Portugal: Faculdade de Engenharia da Universidade do Porto*, 2014.
[18] T Raveh Tilleman, MM Tilleman, and HAM Neumann. The elastic properties of cancerous skin: Poisson's ratio and Young's modulus. Optimization of Incisions in Cutaneous Surgery including Mohs' Micrographic Surgery., page 105, 2004.
[19] Guangyao Liu, Qiao Zhang, Yan Jin, and Zhongli Gao. Stress and strain analysis on the anastomosis site sutured with either epineurial or perineurial sutures after simulation of sciatic nerve injury. *Neural regeneration research*, 7(29):2299, 2012.

Journal of Computation and Artificial Intelligence in Mechanics and Biomechanics ISSN 2184-8971
Volume 1, Issue 2, Page 48-57, 2021

Biomechanical study of the shoulder joint complex and associated injuries

Catarina Silva [1], João Ferreira [2], Marco Parente [3]

[1] *catarinasousassilva@gmail.com; Faculty of Engineering, University of Porto; Porto; Portugal*
[2] *j.ferreira@fe.up.pt; Faculty of Engineering, University of Porto; Porto; Portugal*
[3] *mparente@fe.up.pt; Science and Innovation in Mechanical and Industrial Engineering; Porto; Portugal*

Abstract

The glenohumeral joint allows the arm to perform countless and varied movements. This diversity generates a vulnerability on the joint, which, in turn, tends to suffer dislocations, affecting 1-2% of the population. In addition, individuals who frequently perform activities such as swimming, baseball, tennis, among others, are more likely to have shoulder injuries due to the stress to which their joints and muscles are subjected. It is also known that, given a first dislocation, it may lead to the appearance of lesions in the structures that make up the shoulder joint complex, causing some patients to suffer from recurrent dislocations. This can be due to the inaccurate information available regarding the most appropriate treatment for each situation. It is important to note that a proper treatment should allow the patient to regain glenohumeral joint stability without causing pain and reducing mobility. The development of this work aims to contribute to a better understanding of the shoulder complex, and thus provide relevant clinical information, allowing clinicians to perceive the most appropriate treatments with greater ease and confidence, ensuring that the patient will not suffer from instability in the glenohumeral joint again. A finite element model was built for this study, which allowed a biomechanical analysis of the shoulder complex. This work allowed to verify the importance of the stabilizing role of the glenohumeral ligaments with the humerus positioned in the upper ranges. In addition, it was possible to conclude that glenoid defects with sizes greater than 37.5% of the glenoid width combined with any defect in the humeral head should be repaired with a Latarjet procedure.

***DOI**: 10.5281/zenodo.4843511*

Article Info

Keywords
Finite element method
Anterior dislocation
Bankart lesions
Hill-Sachs lesions
Biomechanics

Article History
Received: *12/01/2021*
Revised: *26/03/2021*
Accepted: *05/05/2021*

1 Introduction

The shoulder enables the performance of a wide range of different movements such as flexion, extension, abduction, adduction, external and internal rotation. In case any of its structures gets injured, it can lead to weakness, pain or instability [1]. It has been reported that 1-2% of the general population will experience a glenohumeral dislocation [2]. Besides, it was reported that glenohumeral dislocations in the anterior direction correspond to 98% of all shoulder dislocations [3].

Bankart and Hill-Sachs lesions result from anterior dislocations and are quite individualized, which means that these can have different sizes and locations. Besides, there is also a wide variety of treatments and little certainty as to which will be the most suitable for each situation. Consequently, the recurrence rate for the treatment including immobilization and physical therapy can exceed 70%, and the recurrence rate following surgical repair has been reported to be up to 17.5%. In addition, for patients that are subjected to surgical repair, these may experience joint stiffness and reduced range of motion [4].

The aim of this work is to better understand the mechanisms of the shoulder complex and the aetiology of shoulder instability, attempting to establish a validated algorithm that makes it easier to choose the most appropriate treatment for each situation, providing stability without limiting the range of motion and, consequently, decreasing the recurrence rates. More specifically, it focuses on evaluating the stability of the glenohumeral joint with the presence of the Bankart and Hill-Sachs defects simultaneously, since it was reported that the recurrence is usually associated with the presence of both lesions [5].

Corresponding Author:
Catarina Silva
catarinasousassilva@gmail.com

1.1. Bankart and Hill-Sachs lesions

Anterior dislocations usually occur with the humerus in the apprehension position (60º abducted and 60º externally rotated) [6]. These may lead to permanent deformation of the glenohumeral ligaments, antero-inferior labral lesions and bony injuries that consequently result in recurrent instability.

A Bankart lesion consists of the detachment of the antero-inferior section of the labrum and may also involve bone loss. A study reported that these lesions occur in up to 95% of the shoulders that had a dislocation [7].

Another common shoulder injury is the Hill-Sachs lesion which can be defined as a cortical depression in the postero-superior section of the humeral head. These were reported to occur in up to 90% of shoulders that had a dislocation [7].

1.2. Treatments

Treatment may involve non-surgical rehabilitation or surgical repair. The first approach usually involves an immobilization period of approximately 3 weeks and it is followed by a rehabilitation period, in which the patient gradually returns to daily activities [8]. Surgical techniques are used when the injury is more severe, and these include anatomic or intracapsular repairs, which attempt to repair and reinsert the labrum and the ligaments in their original position (e.g. Bankart repair) and nonanatomic or extracapsular repairs, which consist of reconstructing the glenohumeral joint with a bone block (e.g. Bristow or Latarjet procedures) or with a soft tissue block (e.g. Putti–Platt or Magnuson–Stack procedures) [9].

Worldwide, Bankart repair accounts for almost 90% of primary surgeries for anterior instability. However, in France 72% of surgeons prefer the Latarjet repair as a primary surgery for instability [4].

Besides, the current literature lacks comprehensive comparative studies, in other words, there are studies suggesting that glenoid critical bone loss should be lower than 20% of the glenoid width [10], while others suggest that it is 21% [11] and 25% [12]. Regarding Hill-Sachs defects, while a study suggests that it is recommended treatment for defects with sizes bigger than 37.5% of the diameter of the humeral head [13], another suggests treatment for defects with size greater than 31.25% [14]. Finally, for combined defects, a study suggested that at least one of the defects should be addressed with a bony reconstruction for defects of 10-20% of the glenoid width combined with defects of 19% of the humeral head diameter [3]. It was also reported that a bony procedure should be performed when there is a glenoid bone loss greater than 20% and an engaging Hill-Sachs lesion [15]. In addition, [16] suggested that glenoid defects smaller than 25% combined with a non-engaging Hill-Sachs lesion should undergo arthroscopic Bankart repair, while if combined with an engaging Hill-Sachs lesion the patient should also be subjected to a *remplissage*; If the glenoid defects are greater than 25% a Latarjet procedure should be performed for a non-engaging Hill-Sachs lesion, and a Latarjet combined with a *remplissage*/bone graft should be performed for an engaging Hill-Sachs lesion.

2 Methodology

To determine the effect of combined injuries in shoulder stability, a finite element model was created. This model includes the humerus, the scapula and their respective cartilages as done by Walia et al, 15 [17]. Besides, it was added the synovial liquid and the glenohumeral capsule and ligaments.

From a set of medical images obtained from CT (computerized tomography), 3D models of the humerus and the scapula were created, using the Mimics software (v20).

Then, the model was imported into the 3-Matic software (v12) to create the mesh. It is known that as the size of finite elements tends to zero, the solution obtained converges to the exact solution. However, in order not to get too heavy files, a mesh with triangles with sides measuring approximately 0.0025 m was created and the surfaces of the glenoid and humeral head that will have contact conditions have been assigned with a more refined mesh (0.0014 m).

In Femap (v11.4.1) the articular cartilages were modelled. The main function of cartilage is to reduce friction and promote good contact between the bones. Cartilage was created as having a thickness of 0.0015 m, however since the thickness of the cartilage on the humeral head and glenoid is not uniform, the simulations will begin by promoting the fit between these two surfaces.

Solidworks was used to construct the structure of the glenohumeral capsule. According to literature, it is more appropriate to consider the capsule as a continuous sheet, instead of several discrete structures [18].

The mesh of the capsule was created in Abaqus (2019). As shown in Fig.1 the posterior section has only one layer (red) since it is thinner, and the section of the capsule which is reinforced by the ligaments has two layers (red and blue). After the mesh was ready, pressure was applied to the inferior section of the capsule to recreate the insertion of the IGHL (Inferior Glenohumeral Ligament) into the anatomical neck of the humerus in a U- or V- shape, as shown in Fig. 1.

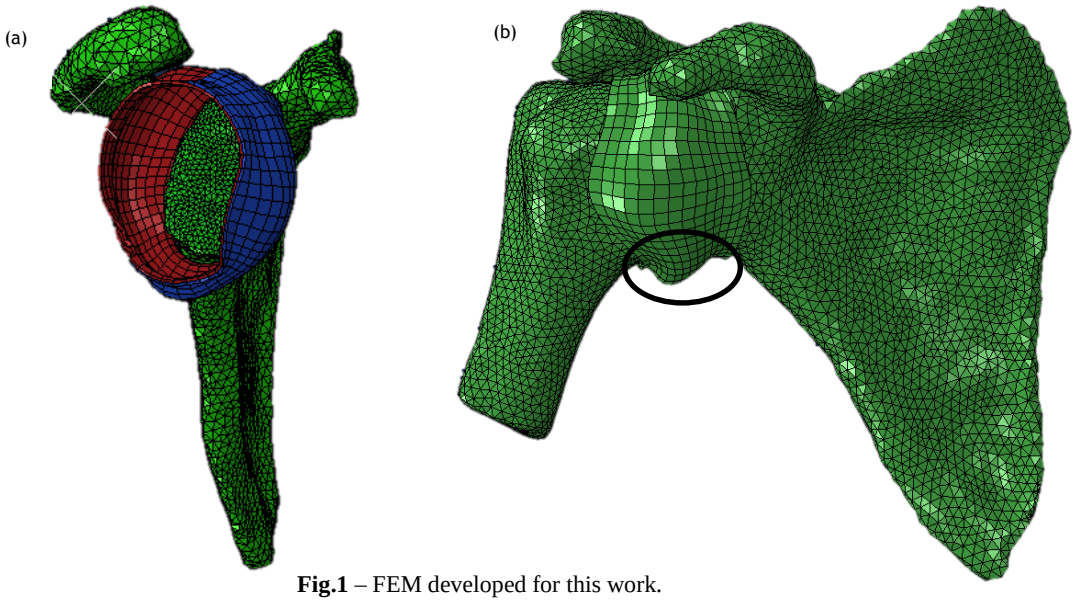

Fig.1 – FEM developed for this work.

The positions that were chosen as the initial positions to run the simulations were with the humerus at 45º or 90º humero-thoracic abduction and neutral rotation, 40º of external rotation or 60º external rotation.

2.1. Creation of defects

The size of the defects was chosen based on [3] for the humeral head and [11] for the glenoid and are shown in table 1 and the defects made are shown in Fig. 2.

Table 1 – Sizes of the defects

	Humerus defect size (% of the diameter of the humeral head)	Glenoid defect size (% of the glenoid width)
Defect 1	0.00238 m (6%)	0.00434 m (12,5%)
Defect 2	0.00753 m (19%)	0.00868 m (25%)
Defect 3	0.01228 m (31%)	0.01302 m (37,5%)
Defect 4	0.01743 m (44%)	0.01736 m (50%)

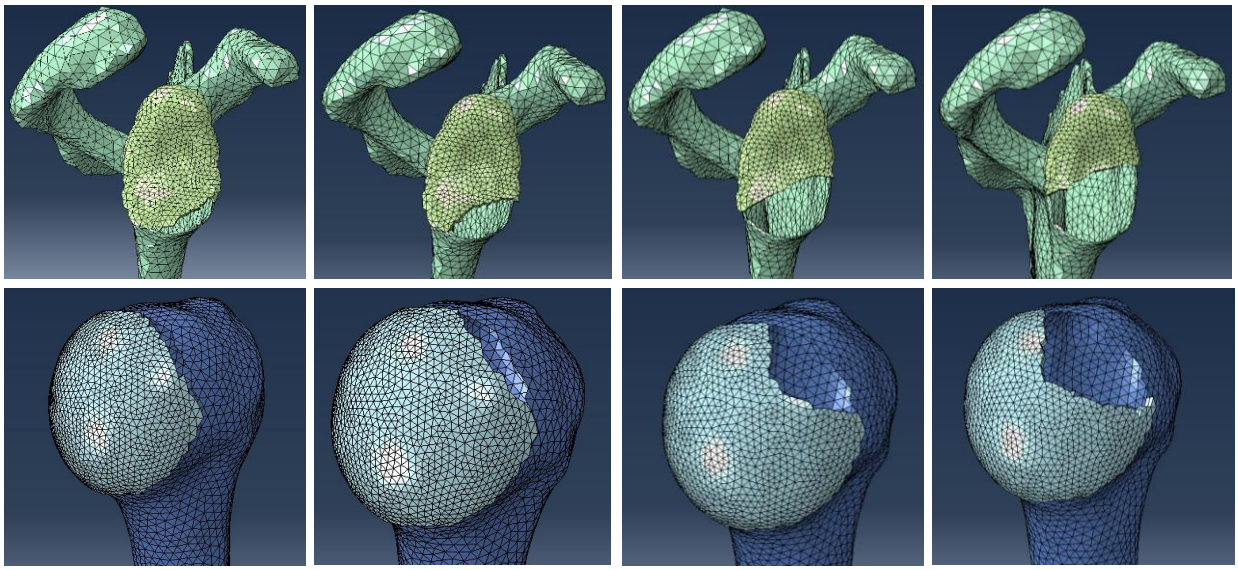

Fig. 2 – Bankart and Hill-Sachs defects created in this work.

2.2. Material Properties

Bones were assumed to be rigid bodies since bone deformation is almost negligible when compared to soft tissues and to reduce computational cost, while the articular cartilage was modelled as a Neo-Hookean hyperelastic, incompressible material [17], [19].

To study the behaviour of glenohumeral ligaments and following the suggestions of previous studies [18], a hyperelastic constitutive model - Holzapfel-Gasser-Ogden (HGO) - was used. Besides, it was added a numerical damage parameter to represent the behaviour of the ligaments more accurately.

In the HGO model, the strain energy density function is defined as:

$$\Psi = \Psi_{vol} + \Psi_{mat} + \Psi_{fib} \tag{1}$$

where $\boldsymbol{\Psi_{mat}}$ corresponds to the contribution of the matrix, $\boldsymbol{\Psi_{fib}}$ corresponds to the contribution of the fibers and $\boldsymbol{\Psi_{vol}}$ imposes the incompressible behaviour of the material.

More, $\boldsymbol{\Psi_{vol}}, \boldsymbol{\Psi_{mat}}, \boldsymbol{\Psi_{fib}}$ are expressed as:

$$\Psi_{\mathrm{vol}} = \frac{1}{\mathrm{D}}\left(\frac{\left(\mathrm{J}^{\mathrm{el}}\right)^2 - 1}{2} - \ln \mathrm{J}^{\mathrm{el}}\right) \tag{2}$$

$$\Psi_{\mathrm{mat}} = \mathrm{C}_{10}(\bar{\mathrm{I}}_1 - 3) \tag{3}$$

$$\Psi_{fib} = \frac{k_1}{2k_2}\sum_{\alpha=1}^{N}\{\exp[k_2\langle\bar{E}_\alpha\rangle^2] - 1\} \tag{4}$$

with

$$\bar{E}_\alpha = k(\bar{I}_1 - 3) + (1 - 3k)\left(\bar{I}_{4(\alpha\alpha)} - 1\right), \tag{5}$$

where $\mathbf{C_{10}}$, $\mathbf{D}$, $\boldsymbol{k_1}$ and $\boldsymbol{k_2}$ are material coefficients.

$\boldsymbol{N}$ is the number of fiber families, which was assumed in this work to be $N = 1$, and $\boldsymbol{k}$ is a parameter that controls the dispersion of the fibers around the mean direction (it can have a value between 0 and 1/3 - if $\boldsymbol{k}$ = 0 it means the fibres are perfectly aligned in the preferential direction, whereas if $\boldsymbol{k}$ = 1/3 it means that the fibres are randomly distributed).

$\boldsymbol{\bar{I}_1}$ is the first strain invariant and $\boldsymbol{\bar{I}_{4(\alpha\alpha)}}$ are pseudo-invariants of the deviatoric part of the right Cauchy-Green deformation tensor.

To define the preferential direction of the fibres it was adapted a Matlab routine from [20]. This created a vector at the centroid of each element defining the orientation of the fibres.

The HGO constitutive model, despite describing the material properties of the ligaments, is limited to the range of physiological loads. Therefore, in order to represent the ligaments more accurately, it should be considered the non-physiological loads, which cause soft tissues to damage arising from the tear or plastic deformation of the fibres. So, a model that describes the reduction in the mechanical stiffness of ligaments when non-physiological strains lead to progressive failure of the fibres was used [21]:

$$\Psi = \Psi_{vol} + (1 - D_m)\Psi_{mat} + \left(1 - D_f\right)\Psi_{fib} \tag{6}$$

where $\boldsymbol{D_m} \epsilon [0,1]$ is the damage variable for the matrix and $\boldsymbol{D_f} \epsilon [0,1]$ is the damage variable for the fibers. Table 2 shows the parameters used in this work.

Table 2 – Material Properties.

	Type	Parameters	Number of elements (Element type)
Humerus	Rigid body	-	5662 (S4R)
Scapula	Rigid body	-	19775 (S4R)
Articular cartilage	Hyper-elasticity	$C_{10} \approx 1.79$ MPa	5650 (C3D6H)
Glenohumeral capsule	Hyper-elasticity	$C_{10} = 3.82^{-1}$ MPa $k_1 = 1^{-4}$ MPa $k_2 = 5^{-3}$ $k = 5^{-3}$ $\psi^f_{\max} = 3.15^{-1}\sqrt{MPa}$ $\psi^f_{\min} = 5^{-4}\sqrt{MPa}$	1048(C3D8H)

2.3. Simulations

Simulations were run in the presence of bipolar lesions and these comprised 3 steps: pre-tension, contact and translation. Since the capsule only acts as a stabilizer of the glenohumeral joint when it is under tension [11], the pre-tension step was to ensure this. In the initial position the cartilages are inside each other, and with the stretching of the capsule, the cartilages separate, creating tension in the capsule. Then, the contact between the two cartilages was promoted, moving the humerus in the medial direction and restricting all other movements. In the final step, the humeral head was translated in the antero-inferior direction (x-axis), and rotation was restricted in all axis. During all the steps of the simulation the scapula was considered static.

3 Results

In order to conclude regarding the size of defects that lead to shoulder dislocation, the distance to dislocation (DTD) and the Stability Ratio were evaluated, as previously done in other studies [3], [17].

The figures below show the DTD obtained for the different positions tested and with different defects combined.

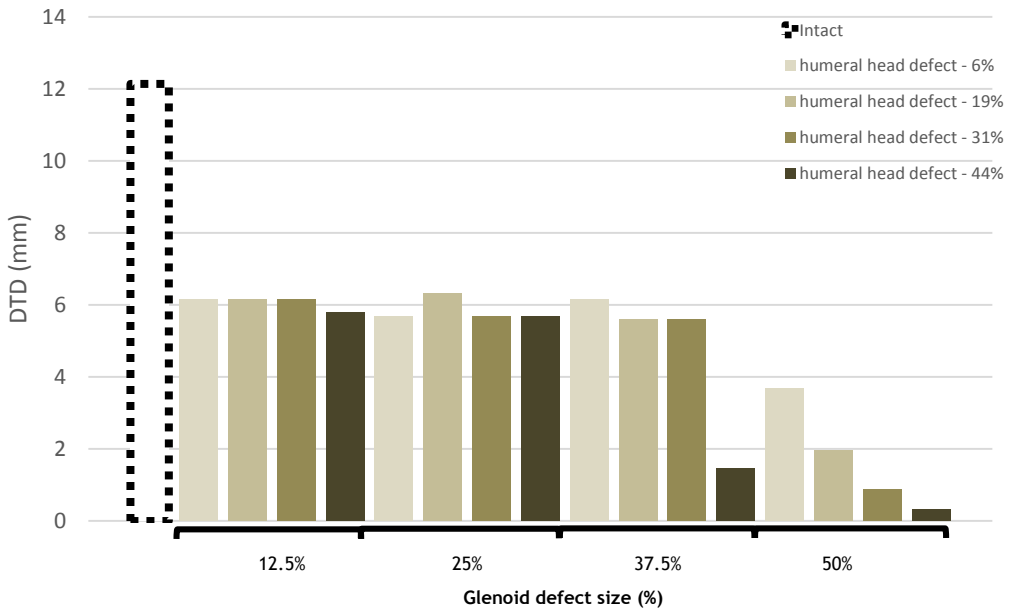

Fig. 3 – DTD for the different combination of defects for the humerus with 45º of abduction and Neutral Rotation.

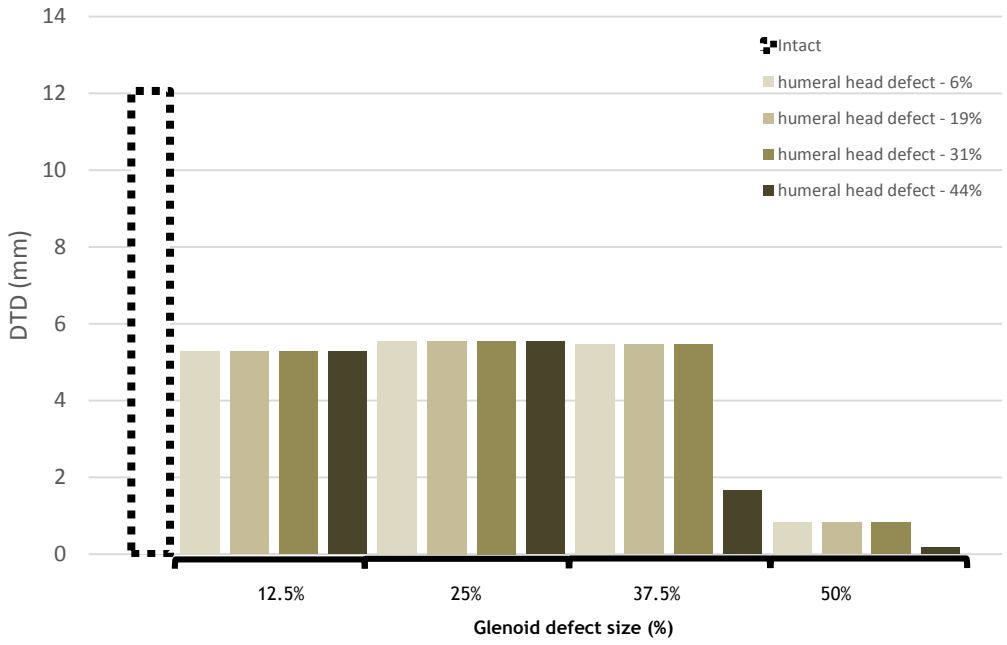

Fig. 4 – DTD for the different combination of defects for the humerus with 90º of abduction and Neutral Rotation.

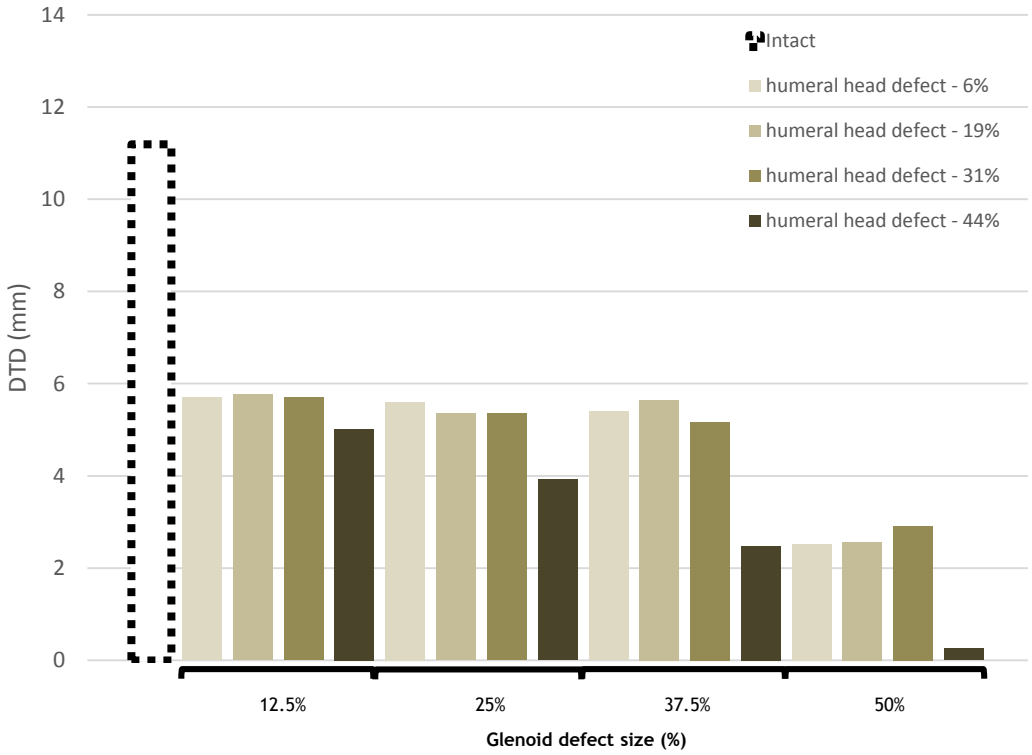

Fig. 5 – DTD for the different combination of defects for the humerus with 45º abduction and 40º of external rotation.

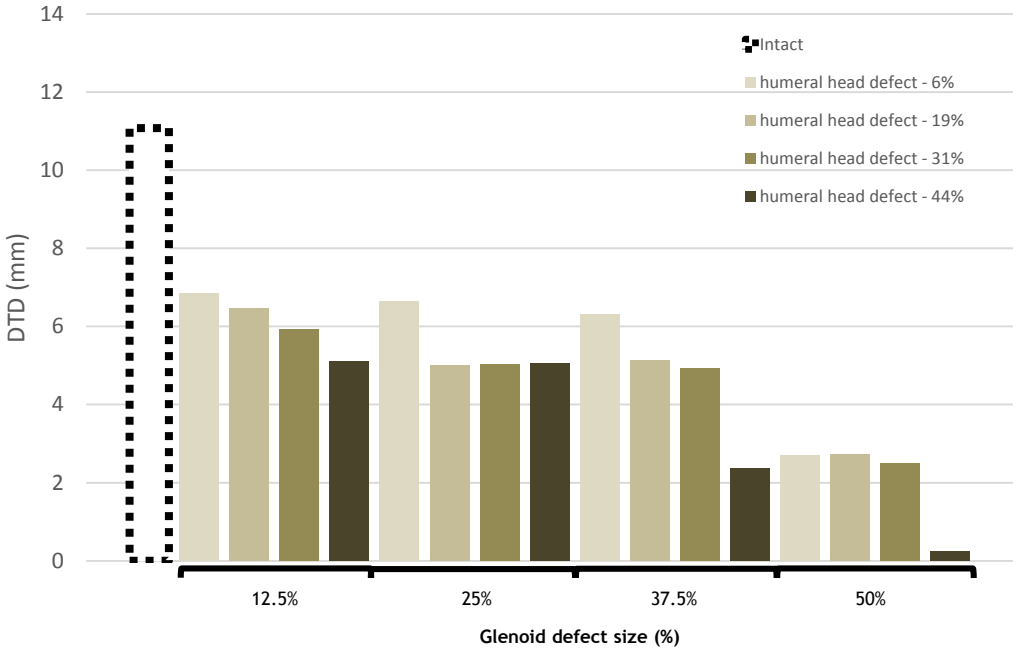

Fig. 6 – DTD for the different combination of defects for the humerus with 45º abduction and 60º of external rotation.

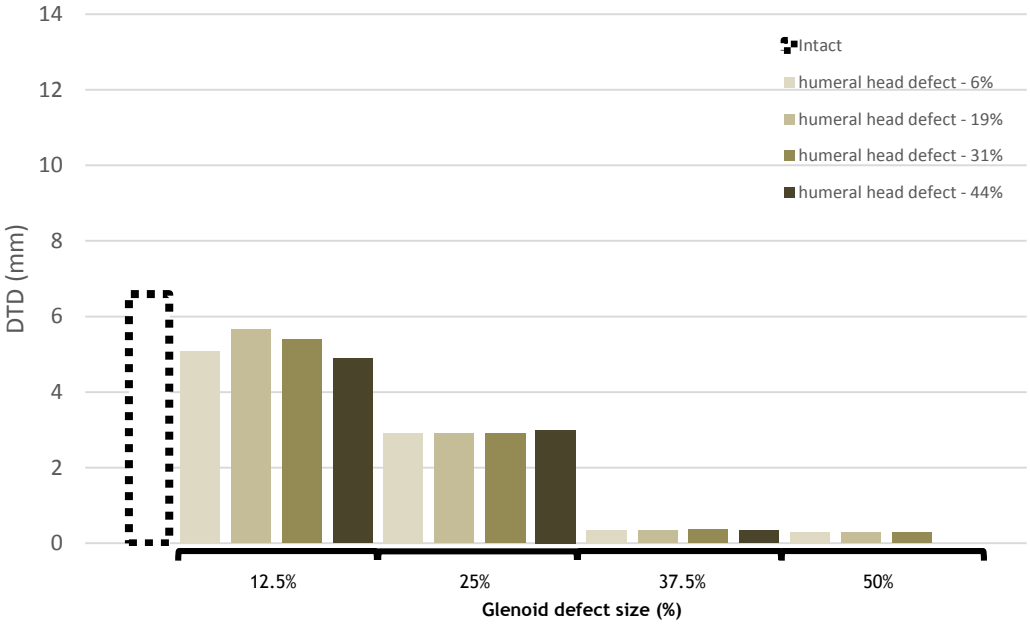

Fig. 7 – DTD for the different combination of defects for the humerus with 90º abduction and 40º of external rotation.

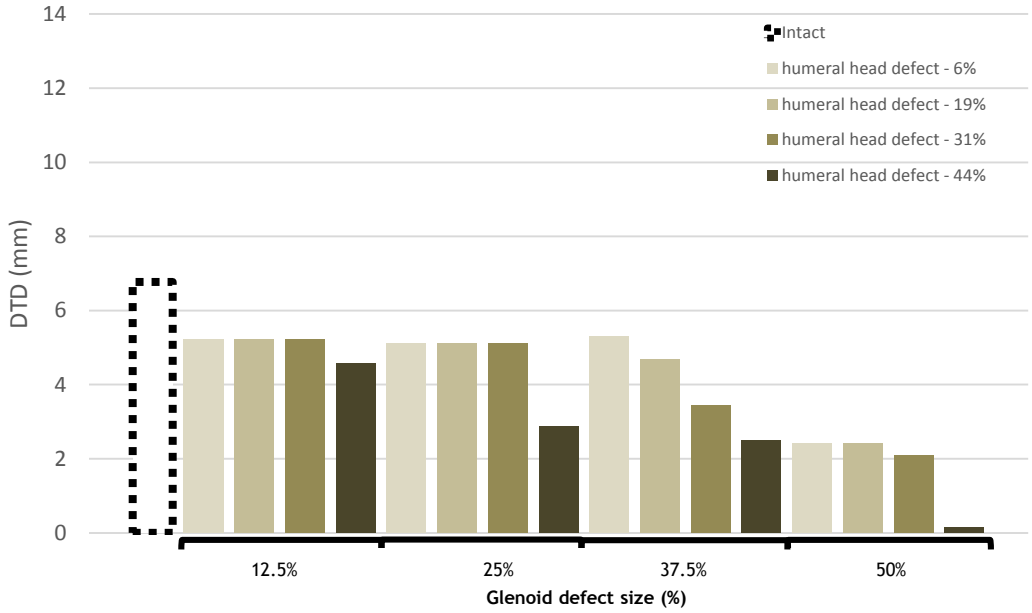

Fig. 8 – DTD for the different combination of defects for the humerus with 90º abduction and 60º of external rotation.

For the humerus abducted 45º/90º and with neutral rotation, the DTD is approximately the same for all defects, except for the glenoid defect of 50% combined with any humeral head defect and the glenoid defect of 37.5% combined with a humeral head defect of 44%. However, the DTD for the humerus with 45º abduction is about 0.006 m and for 90º it is about 0.005 m. Therefore, it can be concluded that the humerus is more unstable for higher abduction angles.

When the humerus is externally rotated with 45º of abduction, Hill-Sachs defects have a greater influence on the stability as the external rotation angle increases. But, in general, the DTD did not present very distinct differences between the external rotation of 40º and 60º.

Moreover, when the humerus is externally rotated at 90º of abduction, different data were obtained from what is presented in the literature. In other words, the DTD for the humerus externally rotated 60º was bigger for the glenoid defect of 25% of the glenoid width when compared with DTD obtained for the humerus externally rotated 40º. This can be justified by the fact that it was considered the presence of ligaments, which stabilize the shoulder in upper ranges.

In summary, when the humerus was with neutral rotation, the size of the glenoid defect was the main cause for instability, while the humeral head defects had more influence when the humerus was externally rotated. Therefore, it can be concluded that the glenoid defects lead to translational instability while the humeral head defects lead to rotational defects, as it was also concluded in another study [17].

Moreover, it can be concluded that the influence of Hill-Sachs defects on glenohumeral stability not only depends on its size but also on its location. Therefore, it is important to note that if another method was used to create the defects, the results might have been different.

To evaluate the stability of the glenohumeral joint, it was calculated the stability ratio (r):

$$r = \frac{s}{c} \tag{7}$$

where the compressive force (c) was considered as the force of the humerus against the glenoid during the contact step and the translational force (s) was considered as the force on the humerus that allows its translation in the anterior-inferior direction until a dislocation or subluxation occurs.

The table below shows the stability ratio obtained for each case:

Table 3 - Stability Ratio for combined defects at 45º and 90º.

	Humeral Head Defects				
Glenoid defects (45º)	Intact	6%	19%	31%	44%
Intact	0.49	-	-	-	-
12.5%	-	0.40	0.40	0.40	0.40
25%	-	0.18	0.18	0.18	0.12
37.5%	-	0.11	0.10	0.08	0.08
50%	-	0.08	0.08	0.05	0
Glenoid defects (90º)	Intact	6%	19%	31%	44%
Intact	0.47	-	-	-	-
12.5%	-	0.26	0.26	0.26	0.26
25%	-	0.14	0.14	0.14	0.13
37.5%	-	0.12	0.12	0.13	0.11
50%	-	0	0	0	0

For a joint without defects, the ratio of 47% and 49% for the abduction angles of 90° and 45°, was obtained, respectively. These values are similar to the ratio of 43% and 44% obtained in the study [22].

It was concluded from these results that the stability ratio did not show big differences as the size of the Hill-Sachs defects got bigger and the obtained values also confirm the fact that the stability of the joint decreases with the increase in the size of the defects. Besides, these values also support the fact that for larger abduction angles the joint is more unstable.

4 Conclusions

The outputs from this work allowed us to conclude that glenoid defects with sizes bigger than 37.5% of the glenoid width can easily lead to shoulder dislocation. So, a bone block on the glenoid should be performed to recover the glenohumeral joint stability. For glenoid defects with sizes between 12.5% and 37.5%, a Bankart repair might be able to restore stability. Finally, a *remplissage* might be recommended to address humeral head defects with sizes bigger than 44%.

It is also important to note that, as in other studies, the creation of the defects took into consideration the same orientation for all the defects. Although this allows reproducibility, it has the limitation of not representing clinical defects.

For future work, it is suggested to add the muscles to the model and evaluate their influence. This, assuming that if the ligaments have been shown to increase stability on upper ranges of abduction, then the muscles may increase stability in the mid- ranges. Besides, the addition of labrum should also contribute to increased stability since it accounts for 10-20% of the stabilizing forces.

References

[1] Metan SS, Krishna P, Mohankumar GC. FEM Model an Effective Tool to Evaluate Von Mises Stresses in Shoulder Joint and Muscles for Adduction and Abduction. Procedia Materials Science. 2014;5:2090-8.

[2] Varacallo M, Musto MA, Mair SD. Anterior Shoulder Instability. [Updated 2020 Mar 13]. In: StatPearls [Internet]. Treasure Island (FL): StatPearls Publishing; 2020 Jan-.

[3] Gottschalk LJ 4th, Walia P, Patel RM, Kuklis M, Jones MH, Fening SD, Miniaci A. Stability of the Glenohumeral Joint With Combined Humeral Head and Glenoid Defects: A Cadaveric Study. Am J Sports Med. 2016 Apr;44(4):933-40.

[4] Hardy A, Sabatier V, Laboudie P, Schoch B, Nourissat G, Valenti P, Kany J, Deranlot J, Solignac N, Hardy P, Vigan M, Werthel JD. Outcomes After Latarjet Procedure: Patients With First-Time Versus Recurrent Dislocations. Am J Sports Med. 2020 Jan;48(1):21-26.

[5] Nakagawa S, Ozaki R, Take Y, Iuchi R, Mae T. Relationship Between Glenoid Defects and Hill-Sachs Lesions in Shoulders With Traumatic Anterior Instability. Am J Sports Med. 2015 Nov;43(11):2763-73.

[6] Browe DP, Voycheck CA, McMahon PJ, Debski RE. Changes to the mechanical properties of the glenohumeral capsule during anterior dislocation. J Biomech. 2014 Jan 22;47(2):464-9.

[7] Taylor DC, Arciero RA. Pathologic changes associated with shoulder dislocations. Arthroscopic and physical examination findings in first-time, traumatic anterior dislocations. Am J Sports Med. 1997 May-Jun;25(3):306-11.

[8] Pogorzelski J, Fritz EM, Godin JA, Imhoff AB, Millett PJ. Nonoperative treatment of five common shoulder injuries: A critical analysis. Obere Extrem. 2018;13(2):89-97.

[9] Trofa D, Hsu AC, Levine WN. 13 - Persistent anterior shoulder instability following surgical stabilization. Shoulder and Elbow Trauma and its Complications, R. M. Greiwe, Woodhead Publishing, 271-90, 2015.

[10] Shaha JS, Cook JB, Song DJ, Rowles DJ, Bottoni CR, Shaha SH, Tokish JM. Redefining "Critical" Bone Loss in Shoulder Instability: Functional Outcomes Worsen With "Subcritical" Bone Loss. Am J Sports Med. 2015 Jul;43(7):1719-25.
[11] Itoi E, Lee SB, Berglund LJ, Berge LL, An KN. The effect of a glenoid defect on anteroinferior stability of the shoulder after Bankart repair: a cadaveric study. J Bone Joint Surg Am. 2000 Jan;82(1):35-46.
[12] Garcia GH, Wu HH, Liu JN, Huffman GR, Kelly JD 4th. Outcomes of the Remplissage Procedure and Its Effects on Return to Sports: Average 5-Year Follow-up. Am J Sports Med. 2016 May;44(5):1124-30.
[13] Sekiya JK, Wickwire AC, Stehle JH, Debski RE. Hill-Sachs defects and repair using osteoarticular allograft transplantation: biomechanical analysis using a joint compression model. Am J Sports Med. 2009 Dec;37(12):2459-66.
[14] Kaar SG, Fening SD, Jones MH, Colbrunn RW, Miniaci A. Effect of humeral head defect size on glenohumeral stability: a cadaveric study of simulated Hill-Sachs defects. Am J Sports Med. 2010 Mar;38(3):594-9.
[15] Bollier MJ, Arciero R. Management of glenoid and humeral bone loss. Sports Med Arthrosc Rev. 2010 Sep;18(3):140-8.
[16] Milano G, Frizziero G, Marchi G. Bony Defects: Glenoid and Humeral Side—On-Track/Off-Track Concept. In: Brzóska R, Milano G, Randelli P, Kovačič L. (eds) 360° Around Shoulder Instability. Springer, Berlin, Heidelberg, 2020.
[17] Walia P, Miniaci A, Jones MH, Fening SD. Influence of Combined Hill-Sachs and Bony Bankart Defects on Range of Motion in Anterior Instability of the Shoulder in a Finite Element Model. Arthroscopy. 2015 Nov;31(11):2119-27.
[18] Moore SM, Ellis B, Weiss JA, McMahon PJ, Debski RE. The glenohumeral capsule should be evaluated as a sheet of fibrous tissue: a validated finite element model. Ann Biomed Eng. 2010 Jan;38(1):66-76.
[19] Zheng M, Zou Z, Bartolo PJ, Peach C, Ren L. Finite element models of the human shoulder complex: a review of their clinical implications and modelling techniques. Int J Numer Method Biomed Eng. 2017 Feb;33(2):e02777.
[20] Fonseca MC. Biomechanical Simulation of the Damage on the ACL in Injury Related Movements. MS, Faculdade de Engenharia, Universidade do Porto, 2020.
[21] Calvo B, Peña E, Martinez MA, Doblaré M. An uncoupled directional damage model for fibred biological soft tissues. Formulation and computational aspects. International Journal for Numerical Methods in Engineering. 2007;69:2036-57.
[22] Walia P, Miniaci A, Jones MH, Fening SD. Theoretical model of the effect of combined glenohumeral bone defects on anterior shoulder instability: a finite element approach. J Orthop Res. 2013 Apr;31(4):601-7.